



POLITECNICO DI TORINO

Course of Civil Engineering

Master's Degree Thesis

**Cohesive and Overlapping Crack Models:
Application to steel bar reinforced or
pre-stressed concrete structural elements**

Tutors:

Prof. Alberto Carpinteri

Dr. Federico Accornero

Candidate:

Renato CAFARELLI

ACADEMIC YEAR 2018-2019

Acknowledgements

The candidate wishes to express his thanks to Prof. Alberto Carpinteri and Dr. Federico Accornero for their support in the realization of this Thesis.

Abstract

Since the pioneering work of Griffith (1920), it is clear that in order to study the strength of materials it is necessary to take into account the fracture toughness, and the structural scale, in addition to tensile strength. In this way, some short-comings due to traditional structural mechanics models based on stress-strain constitute laws have been understood, and the necessity of a step forward has been pointed out. The Fracture Mechanics approach is a considerable consequence of the design and safety assessment of structures. In the present Thesis, the Cohesive Crack model has been numerically implemented in a new program code in order to study the size effects and the ductile-to-brittle transition of concrete members. More precisely, the cohesive crack model has been adopted to simulate the crack opening in plain or steel bar reinforced concrete elements, whereas the overlapping crack model has been used to simulate the crushing failure of the concrete brittle matrix. Furthermore, in order to take into account the role of the reinforcement layer, a bond-slip law has been utilized referring to considerations reported in Model Code 90.

The present Thesis is divided into five main parts. In the first part, the peculiar aspects and the characteristic parameters of the cohesive crack model and of the overlapping crack model are presented. Numerical algorithms based on these models are described, and some simple applications are illustrated. In the second part, the new program code is introduced and its most important routines are presented in details. In the third part, numerical investigations obtained by

the cohesive/overlapping crack model are presented. Hence, load-deflection curves for several geometries are reported, both for plain or steel bar reinforced concrete elements. Furthermore, in order to assess the algorithm accuracy, a numerical vs. experimental comparison is illustrated. The application of dimensional analysis, which allows to evaluate the minimum and maximum reinforcement ratios, and the rotational capacity of RC beams is recalled: some results obtained by numerical investigations are compared with Code provisions. In the fourth part, a suitable modification of the cohesive/overlapping crack model for pre-stressed concrete structures is introduced, and some numerical case-studies are reported. Finally, some future developments and applications of the cohesive/overlapping crack model are briefly presented.

Contents

List of Tables	IX
List of Figures	X
1 Introduction	1
2 The cohesive model	7
2.1 Basic model concepts	7
2.2 Uniaxial tensile test of a specimen	9
2.3 Three point bending of beams	12
2.4 Carpinteri algorithm	15
2.5 Smearred tip algorithm	19
3 The crushing failure	23
3.1 The Hillerborg model	23
3.2 The overlapping model	24
3.3 Uniaxial compression test of a specimen	28
4 The cohesive/ overlapping algorithm	31
5 The new cohesive/ overlapping algorithm	37
5.1 The routine GUI.mlapp	37
5.2 The routine ReinforcementData.m	39
5.3 The routine master.m	41
5.4 The routine LoadComputation.m	42
5.5 The routine soluz.m	43
5.6 The routine RealTipAdvancement.m	45

6	New algorithm results	47
6.1	Numerical investigation	47
6.2	Parametric analysis and experimental comparison	50
7	Minimum reinforcement	63
7.1	Codes provisions	63
7.2	Numerical models for minimum reinforcement	64
7.3	Dimensional analysis approach	67
8	Rotational capacity of beams	71
8.1	Dimensional analysis approach	73
9	The effect of a pre-stressing force	75
9.1	Numerical investigation	76
10	Future algorithm developments	83
A	Algorithm Variables	85
	Bibliography	89

List of Tables

2.1	Energy brittleness number s_E investigated by Carpinteri	18
6.1	Geometrical characteristics and steel percentages of tested beams .	51
7.1	Mechanical parameters for the beams considered in the numerical simulations	70

List of Figures

1.1	Liberty ship completely divided into two parts	1
1.2	Specimens of different length subjected to a tensile test	3
2.1	Couple of constitutive laws adopted for undamaged (a) and damaged material (b) in tension	7
2.2	Cohesive crack schematization	8
2.3	Different stages of the loading process of a slab subjected to a tensile test	9
2.4	Different post peak stress-displacement response of the specimen. The point U represents a break point for the loading path	11
2.5	Limit condition for a beam in a three points bending test	12
2.6	Loading-deflection diagrams for a ductile and brittle condition in a three point bending geometry	14
2.7	Physical and numerical schemes considered by Carpinteri	15
2.8	Generic situation for the algorithm	17
2.9	Dimensionless load vs. deflection diagrams by varying the brittleness number s_E ($\lambda = 4$, $a_o/b = 0.1$, $\varepsilon_t = 0.87 \cdot 10^{-4}$)	18
2.10	Dimensionless load vs. deflection diagrams by varying the brittleness number s_E ($\lambda = 4$, $a_o/b = 0.3$, $\varepsilon_t = 0.87 \cdot 10^{-4}$)	19
2.11	Dimensionless load vs. deflection diagrams by varying the brittleness number s_E ($\lambda = 4$, $a_o/b = 0.5$, $\varepsilon_t = 0.87 \cdot 10^{-4}$)	19
2.12	Basic linear elastic case for the smeared-tip superposition	20
3.1	Couple of constitutive laws adopted for undamaged (a) and damaged material (b) in compression	25

3.2	Uniaxial compression test on specimens with different dimension and slenderness. S , M , L , denote respectively, small, medium and large specimen	26
3.3	Stages of loading process of a specimen in compression	28
4.1	Forces distribution considered by the cohesive/ overlapping algorithm	32
4.2	Numerical simulation scheme used to compute elastic coefficients of the algorithm	34
4.3	Bond-slip law assumed by MC90	34
4.4	Constitutive laws of steel	35
5.1	User interface of the new algorithm	38
5.2	Steel-concrete interaction	39
5.3	Variables managed by ReinforcementData.m	39
5.4	Pre-stressed steel-concrete interaction	40
5.5	Variables managed by master.m	41
5.6	Function scheme of the routine <i>master.m</i>	42
5.7	Variables managed by LoadComputation.m	43
5.8	Variables managed by soluz.m	43
5.9	Variables managed by RealTipAdvancement.m	45
6.1	Dimensionless load vs. deflection diagrams of plain concrete beams for different geometries, crack lengths and s_E numbers	48
6.2	Dimensionless load vs. rotation diagrams for different geometries and reinforcement ratio	49
6.3	Test machinery adopted by Carpinteri et al.	52
6.4	Numerical (thick curve) vs. experimental curves for specimens from A012-06 to A200-06	54
6.5	Numerical (thick curve) vs. experimental curves for specimens from A012-12 to A100-12	55
6.6	Numerical (thick curve) vs. experimental curves for specimens from A200-12 to A100-18	56
6.7	Numerical (thick curve) vs. experimental curves for specimens from A200-18 to B100-06	57
6.8	Numerical (thick curve) vs. experimental curves for specimens from B200-06 to B200-12	58

6.9	Numerical (thick curve) vs. experimental curves for specimens from C012-06 to C100-06	59
6.10	Numerical (thick curve) vs. experimental curves for specimens from C200-06 to C200-12	60
6.11	Numerical (thick curve) vs. experimental curves for specimens from C012-18 to C200-18	61
7.1	Comparison between minimum reinforcement Codes provisions	65
7.2	Minimum reinforcement vs. effective beam depth according to various models	66
7.3	Minimum reinforcement condition for a beam: $b = t = 400 \text{ mm}$, $\lambda = 4$, $f_{ctm} = 2.2 \text{ mm}$, $G_F = 0.062 \text{ N/mm}$, $E_c = 30 \text{ GPa}$, $\rho = 0.124\%$, $d/b = 0.9$	68
7.4	Best-fit relationship of numerical results in the plane $s-N_{PC}$	69
8.1	ϑ_{PL} definition	72
8.2	ϑ_{PL-x}/d relation according to Eurocode 2	72
8.3	Rotation for different beam heights compared with Eurocode 2 predictions	73
8.4	Rotational capacity comparison	74
9.1	Non-dimensional load vs. rotation for pre-stressing steel having $\rho_p = 0.1\%$ (a) and $\rho_p = 0.2\%$ (b)	77
9.2	Non-dimensional load vs. rotation for pre-stressing beams having $\rho_p = 0.4\%$	78
9.3	Non-dimensional load vs. rotation for pre-stressing beams having $\rho_p = 0.6\%$	79
9.4	Non-dimensional load vs. rotation for pre-stressing beams having $\rho_p = 0.8\%$	80
9.5	Non-dimensional load vs. rotation for pre-stressing beams having $\rho_p = 1.0\%$	81
10.1	Fundamental collapse mechanisms of reinforced concrete beams	84

Chapter 1

Introduction

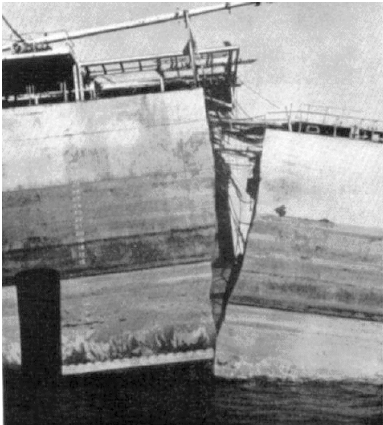


Figure 1.1: Liberty ship completely divided into two parts

The failure of a material may occur in two different ways and indeed, it is possible to distinguish between a *ductile failure* in which material is subjected to plastic, i.e. permanent, deformations or *brittle failure* in which the material breaks itself in a sudden way when it is still within the elastic field. In the recent years, it has been worked out that the behaviour of a material depends also on its size and a new scientific discipline has been setting up to study this topic: the fracture mechanics.

Inglis may be considered the father of this new study field putting out firstly the shortcomings of the classical strength of material theory. Indeed, he solved the problem of an infinite plate having within an ellipsoidal cavity [1]. He observed that the stress approaches infinity at the corners of the cavity, if the ratio of the two ellipse axes tend to infinity i.e. he worked out that the ellipse generates a *stress intensity factor* tending to a crack. A big step forward was made by Griffith [2] who studied the problem of a hole in an infinite plate subjected to an

isotropic stress state. Applying the first law of thermodynamics, he demonstrated that the crack propagates in an unstable manner if the energy variation due a unit propagation of the crack itself overcame the surface energy of the material, i.e. G_F . The work of Griffith represented a revolution in the strength of materials because he highlighted, for the first time, that in order to study the proprieties of a mechanical system is no longer necessary to take into account only stress, but also energy and scale. The note presented at the London Engineering Society was widely appreciated but not completely understood and indeed researches continued to focus their attention on the reconstruction of the stress field around the crack tip by means of the *stress intensity factor* K_{IC} (see [3, 4]) until the World War II and the sudden failure of liberty ships. During this period, the german submarines were sinking the american ships, sent to Allies for supplies, at a rate higher than the speed used by shipyards to construct them. Hence, the American Navy decided to change the construction process changing from a riveting solution to a welding one. However, due to variations in manufacturing techniques, about 400 of 2700 built ships faced fracturing (fig: 1.1). The unexpected failure was caused by several reason [5]:

- weldings were made by a non-professional work force and contained already defects;
- the biggest part of the fractures initiated in correspondence of the hatched corner were *stress concentration* is maximum;
- the steel used was quite poor and did not have high mechanical characteristics.

The liberty ships failure remained a mystery and unresolved for many years and only recently the scale problem has been investigated deeper by means of the definition of the *stress brittleness number* s , by Carpinteri [6, 7] demonstrating that a mechanical systems, having a large characteristic dimensions, tends to behave in a more brittle way. Hence, the strange failure of liberty ships could be understood: plates that are welded together behave as a unique large one and consequently in a more brittle way.

The role of the size effect on the mechanical behavior of a structural system have been nowadays accepted and, more precisely the dependency of the stability of the post peak branch on a characteristic length of the system has been highlighted.

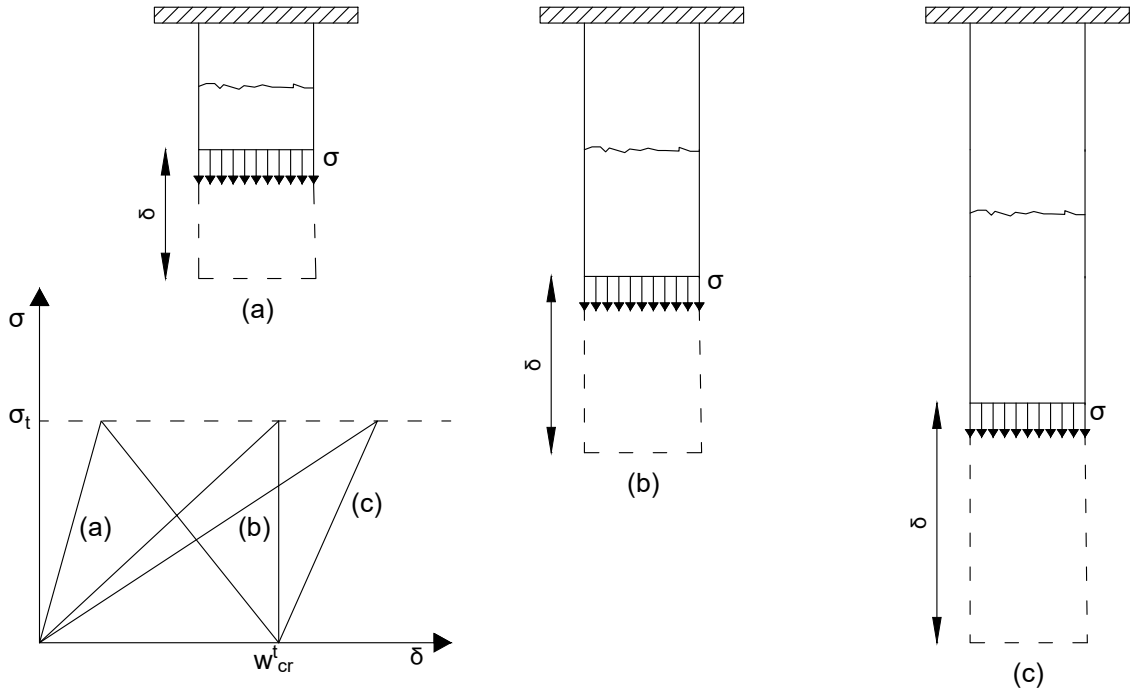


Figure 1.2: Specimens of different length subjected to a tensile test

As an example, it is possible to consider three specimens made of the same material and having three different length as depicted in fig. 1.2 subjected to a tensile test up to their rupture. The load-deflection curves of the specimens are reported in a plane $\sigma - \delta$ where some invariants may be identified:

- the ultimate tensile strength σ_t ;
- the dissipated energy $W_d = G_F \cdot A$, since the specimens have the same cross sectional area;
- the critic displacement value w_{cr}^t for which the rupture occurs.

Hence, the area below the $\sigma - \delta$ curve has to remained constant. However, the specimens present a different rigidity, having a different length, and it is possible to observe a linear positive slope loading path up to σ_t and a post-peak branch depending on the specimen size. Indeed, since the total area described by the three curves is the same, the specimen (a) shows a *softening behavior* with a decrease in the loading carry capacity while, the specimen (b) presents a limit condition for

which once σ_t is reached, there is a vertical dropping for the external load. Meanwhile, the third slab, due its bigger size, exhibits a *snap-back branch* with a decrease both for displacements and load. These three different conditions correspond to a more and more unstable way of acting and, indeed, in order to follow laboratory tests in a stable manner, in the first case the driving parameter has to be the displacement δ while, in the case of the *snap-back*, the test has to be controlled by the crack mouth opening (CMOD).

The size effect is caused by the post-peak strain concentration in a narrow band zone while the other remained part of the specimen is still within the elastic field and, in concrete and more generally concrete-like materials, non-linear phenomena such as detachments, coalescence of micro-voids, microcracking occur [8–11]. The post-peak branch typology and slope is, hence, an essential behavior of the mechanical system and represents a delicate issue in the framework of the the Continuum Mechanics [12–16]. Indeed, it implicates:

- violation of Drucker's Postulate;
- loss of stability in the controlled load condition (*snap-through*);
- loss of stability in the displacement control condition (*snap-back*);
- bifurcation of the equilibrium path;
- loss of the solution in the incremental elasto-plastic response;
- loss of convergence in the numerical analysis.

As regard numerical analysis, attempts to manage these issues were made through the "smeared crack model" [17] in which the stress of the material is limited within the FEM element by the tensile strength. Beyond this threshold value, a drop to zero or a gradually decrease of stress by means of a softening law that depends on the crack opening w^t is introduced. A constitutive law of this typology and defined in the plane $\sigma - w^t$ is called *cohesive law* and, indeed in the zone where strain concentration and energy dissipation occur, material keeps its ability to transfer stress and hence, the fractured band may be modeled assuming a fictitious crack, bigger than the real one, on which faces forces are applied in order to simulate the residual resources of the material. The cohesive model was introduced by Barenblatt [18, 19], reproposeed by Dugdale [20] to study the yielding of metals and

Hillerborg et al. [21] to study the fracturing process of plain concrete members. In the model proposed by Dugdale constant forces were applied on crack faces while in the Hillerborg one, they decrease as the crack width w^t increases and vanish when a threshold value w_{cr}^t is reached.

In the present work, the overlapping model that is formally similar to the cohesive one, is adopted to simulate the compressive failure of concrete and both cohesive and overlapping are adopted to realize a program that is able to simulate the transition in failure mechanisms in concrete structures (plain concrete, reinforced concrete with bars and prestressed members) according to beam depth and steel ratio.

An algorithm built on the integration of the two models has been proposed firstly by Carpinteri et al. [22–28] and Corrado [29] and herein the numerical results presented through years by these two authors are recalled and adopted to validate the new presented algorithm.

Chapter 2

The cohesive model

2.1 Basic model concepts

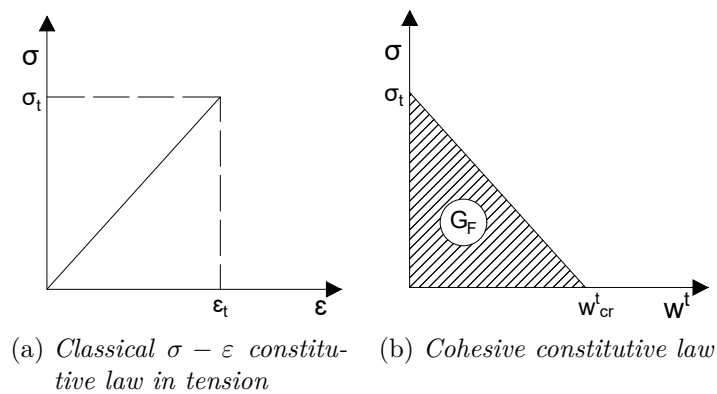


Figure 2.1: Couple of constitutive laws adopted for undamaged (a) and damaged material (b) in tension

The cohesive model has been introduced by Hillerborg et al. [21] and improved by Carpinteri [7, 30] to study the crack formation and growth in concrete. It belongs to strain deformation family models and the assumptions on which it is built are [31]:

- the fracture starts to develop at one point of the specimen when the first principal stress reaches the tensile strength σ_t ;
- the fracture grows perpendicular to the first principal stress;

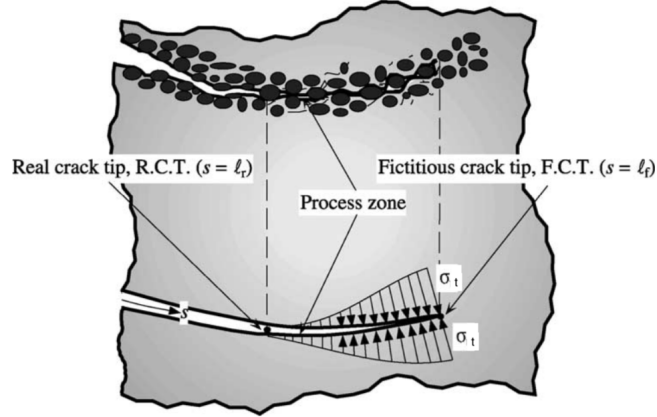


Figure 2.2: Cohesive crack schematization

- the fracture zone is divided into two parts: the zone where the material albeit damaged is still able to transfer stress is called *fictitious crack* and, in the calculation it is replaced by a crack on which faces forces are applied according to a $\sigma - w^t$ relation, i.e. cohesive law as depicted in fig. 2.1b. Meanwhile, the zone on the rear point where the width of the crack reaches the threshold width w_{cr}^t is called *real crack*. Here, the crack faces are in a stress free condition.
- the material outside the fractured zone is assumed to be in the elastic field and a classical $\sigma - \varepsilon$ law is adopted (fig. 2.1a).

In fig. 2.2 a cohesive crack growing within an elastic material in a mode II condition is pictured (shear stress on crack faces are neglected for sake of simplicity). According to model terminology, it is called:

- *fictitious crack tip*, the point where the ultimate tensile strength σ_t of the material is reached;
- *real crack tip*, the point where the threshold value w_{cr}^t is gained;
- *process zone*, the length of the crack along which forces are applied.

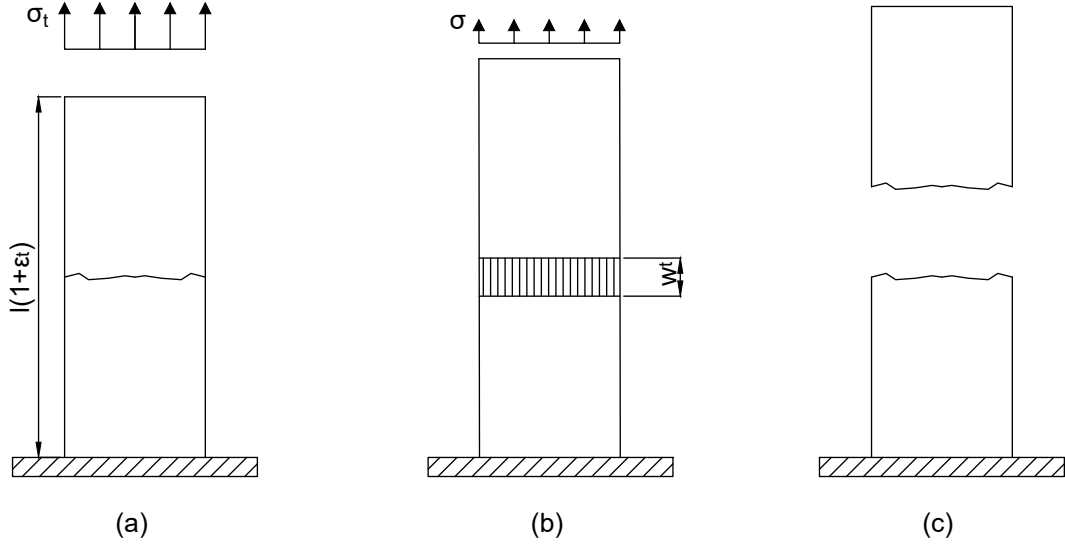


Figure 2.3: Different stages of the loading process of a slab subjected to a tensile test

2.2 Uniaxial tensile test of a specimen

It is possible to consider a specimen made of a quasi-brittle material having the constitutive laws reported in fig. 2.1 that is subjected to a tensile test¹.

$$\sigma = E\varepsilon \quad \varepsilon \leq \varepsilon_t \quad (2.1a)$$

$$\sigma = \sigma_t \left(1 - \frac{w^t}{w_{cr}^t}\right) \quad w \leq w_{cr}^t \quad (2.1b)$$

$$\sigma = 0 \quad w > w_{cr}^t \quad (2.1c)$$

Hence, the specimen will undergo to three different stages as seen in fig. 2.3. In the first step, the mechanical system is within the elastic field and the deformation is proportional to the applied stress by means of the elastic modulus E and the Hook's law. Hence, it is possible to calculate the displacement of the upper edge

¹For sake of simplicity the cohesive law is assumed linear, even though other shapes are possible (e.g. the Model Code 90 [32] suggests to adopt for concrete a bi-linear law).

as:

$$\delta = \frac{\sigma}{E}l \quad \varepsilon \leq \varepsilon_t \quad (2.2)$$

At the peak load, in the weakest section of the system, a fracture develops and a cohesive band is formed while the load decreases. The specimen behaves elastically only outside the fractured zone and thus, the displacement in this stage may be evaluated as:

$$\delta = \frac{\sigma}{E}l + w^t \quad w \leq w_{cr}^t \quad (2.3)$$

Substituting the eqn. 2.1b in eqn. 2.3 it is possible to obtain:

$$\delta = \left(\frac{l}{E} - \frac{w_{cr}^t}{\sigma_t} \right) \sigma + w_{cr}^t \quad w \leq w_{cr}^t \quad (2.4)$$

In a $\delta - \sigma$ plane, the eqn. 2.4 represents a straight line and many cases may occur depending on its slope. Indeed:

- if $w_{cr}^t > \frac{\sigma_t}{E}l$ the slope is negative and a strain softening branch is described (fig. 2.4a);
- if $w_{cr}^t = \frac{\sigma_t}{E}l$ a vertical drop in the load carrying capacity occurs since the slope of the loading path is infinite (fig. 2.4b);
- if $w_{cr}^t < \frac{\sigma_t}{E}l$ a more severe phenomena, i.e. snap-back, takes place decreasing both load and displacement (fig. 2.4c).

The slope that gives the snap-back may be rewrite as:

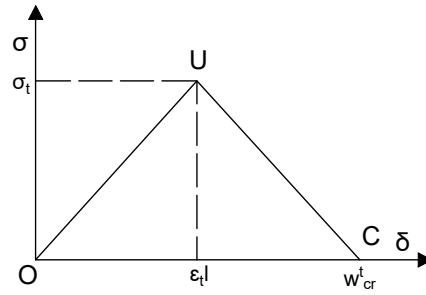
$$\frac{s_E}{\varepsilon_t \lambda} \leq \frac{1}{2} \quad (2.5)$$

where $s_E = \frac{G_E}{\sigma_t b}$ is the *energy brittleness number*, λ is the slenderness ratio of the specimen and b its width.

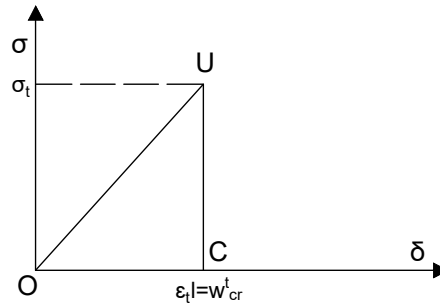
The eqn. 2.5 highlightes a strong relationship between the size of the element and its mechanical behavior and indeed, when the slenderness ratio is larger, the behavior of the system is more brittle. Furthermore, the eqn. 2.5 demonstrates that not the single value of s_E , ε_u and/or λ are responsible of the global behavior of the system but their combination.

Using the previous conditions and assuming for σ_t , E , w_{cr}^t typical average values of concrete, e.g. $\sigma_t = 3 \text{ MPa}$, $E_c = 30000 \text{ MPa}$, $w_{cr}^t = 0.1 \text{ mm}$ it is possible to calculate the minimum length of the concrete specimens corresponding to the softening branch:

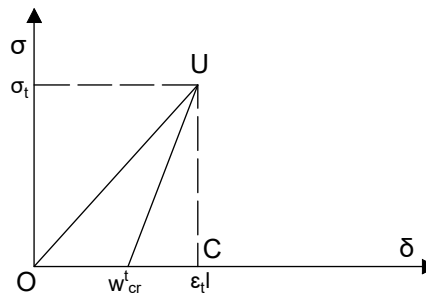
$$l = \frac{w_{cr}^t E}{\sigma_t} = \frac{0.1 \text{ mm} \cdot 30000 \text{ MPa}}{3 \text{ MPa}} = 1000 \text{ mm} \quad (2.6)$$



(a) *Strain softening behaviour*



(b) *Limit condition*



(c) *Snap-back behaviour*

Figure 2.4: Different post peak stress-displacement response of the specimen. The point U represents a break point for the loading path

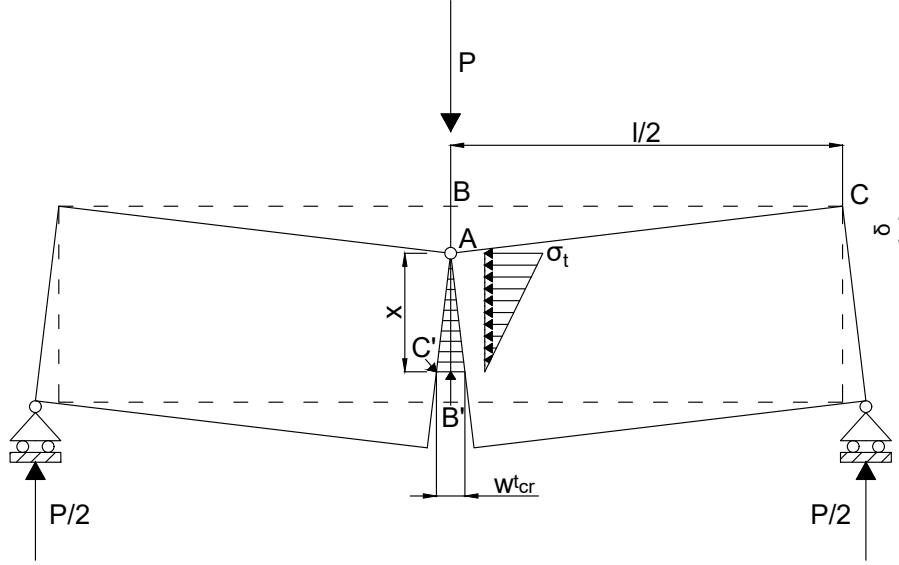


Figure 2.5: Limit condition for a beam in a three points bending test

2.3 Three point bending of beams

From the classical elastic theory, it is known that for a beam in bending the law that relates the load P and the deflection δ is:

$$\delta = \frac{Pl^3}{48EI} \quad (2.7)$$

It is possible to rewrite the eqn. 2.7 in a non-dimensional form:

$$\tilde{P} = \frac{4}{\lambda} \tilde{\delta} \quad (2.8)$$

where the dimensionless load and deflection are respectively:

$$\tilde{P} = \frac{Pl}{\sigma_t t b^2} \quad (2.9)$$

$$\tilde{\delta} = \frac{\delta l}{\varepsilon_t b^2} \quad (2.10)$$

During the loading process, the ultimate tensile strength σ_t is reached at the soffit of the beam and a cohesive crack starts to develop. If the loading process continues, an ultimate condition for the system will be achieved: the beam will

be divided completely in two parts and a cohesive zone of length x will extend towards the extrados of the member as depicted in fig. 2.5 . In this condition, the equilibrium of the system is guaranteed by the external load, the reactions of the bearings and the cohesive forces.

Furthermore, it is possible to write a similitude relation among the triangles ABC and $AB'C'$ in order to find the extension of the process zone x :

$$x = \frac{w_{cr}^t l}{4\delta} \quad (2.11)$$

In order to relate the cohesive forces and the external load P , it is possible to write an equilibrium equation to rotation around the point A for one of the two beams parts:

$$\frac{P l}{2} = \frac{\sigma_t x t}{2} \frac{x}{3} \quad (2.12)$$

Hence, entering the eqn. 2.11 in eqn. 2.12, it is possible to obtain:

$$P = \frac{\sigma_t t / w_{cr}^t}{24} \frac{1}{\delta^2} \quad (2.13)$$

which may be expressed in a non-dimensional form by means of eqn. 2.9, 2.10:

$$\tilde{P} = \frac{1}{6} \left(\frac{s_E \lambda^2}{\varepsilon_t \tilde{\delta}} \right)^2 \quad (2.14)$$

Hence, it is possible to work out two different behaviours for the beam: the eqn. 2.8 is valid until the specimen is within the elastic field, while the hyperbolic eqn. 2.14 represents the asymptotical condition for which the crack propagates through all the beam ligament. According to the classical theory of elasticity, the eqn. 2.8 is valid until:

$$\tilde{P} \leq \frac{2}{3} \quad (2.15)$$

that may be entered in eqn. 2.8, giving:

$$\tilde{\delta} = \tilde{\delta}_1 \leq \frac{\lambda^3}{6} \quad (2.16)$$

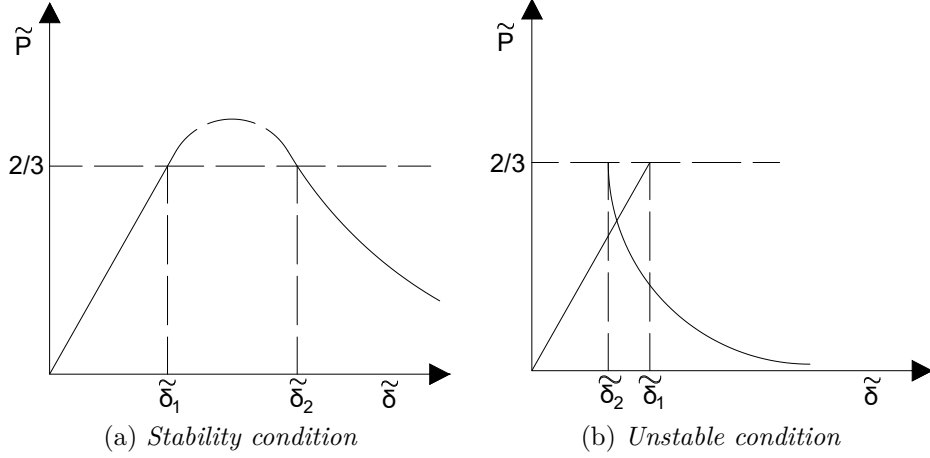


Figure 2.6: Loading-deflection diagrams for a ductile and brittle condition in a three point bending geometry

Whereas, for the application of eqn. 2.14, the following condition should be respected:

$$x \leq b \quad (2.17)$$

Entering the eqn. 2.17 in eqn. 2.12, it is possible to obtain the eqn. 2.15 also for the hyperbolic branch. Entering the eqn. 2.15 in eqn. 2.14, it is possible to have:

$$\tilde{\delta} = \tilde{\delta}_2 \geq \frac{s_E \lambda^2}{2\varepsilon_t} \quad (2.18)$$

It is possible to find out a stability criterion comparing the eqn. 2.16 and eqn. 2.18: if the linear and hyperbolic branches are separated, it is possible to assume that they are connected by a parabola-like curve representing a stable behavior (fig. 2.6a). On the other hand, if the two branches are partially superimposed, it is possible to assume that they are interconnected by a curve having a positive slope, i.e. a snap-back (fig. 2.6).

Hence, the brittleness condition for three point bending loading condition becomes:

$$\frac{s_E}{\varepsilon_u \lambda} \leq \frac{1}{3} \quad (2.19)$$

which is a more severe than eqn. 2.5.

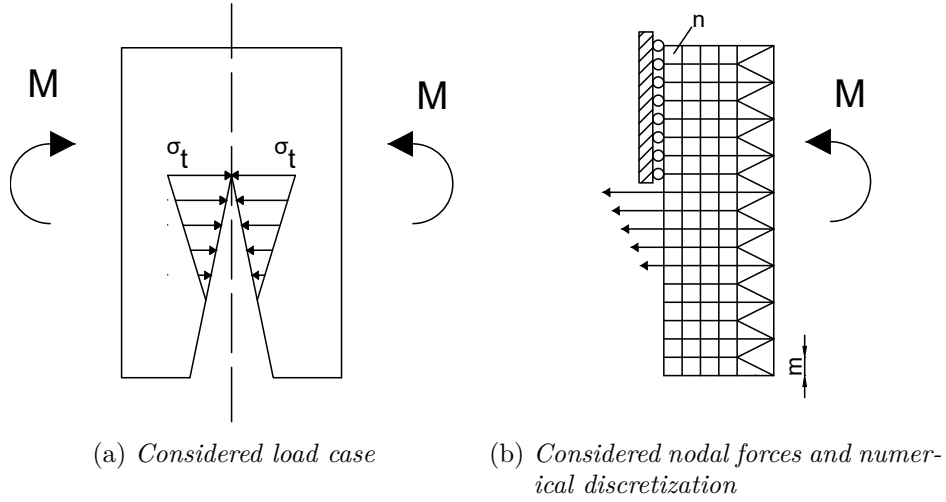


Figure 2.7: Physical and numerical schemes considered by Carpinteri

2.4 Carpinteri algorithm

The numerical algorithm herein presented is based on a FEM approach and, has been proposed by Carpinteri [7, 30] to study the post-peak behavior of plain concrete beams.

The loading process is simulated by means of the incremental advancement of the fictitious crack tip and, hence, the load-deflection curves are obtained through a step-by-step procedure. Moreover, at each step the real crack tip, the external load P and the deflection δ are computed through an iterative computation.

The choice of the discretization domain has to be done according to the analyzed problem in order to avoid numerical and resolution problems. More precisely, as suggested by the author, the condition:

$$m \leq 600 \cdot w_{cr}^t \quad (2.20)$$

where m is the finite element dimension, should be respected.

Considering a three point bending test, the crack opening may be expressed as:

$$\{w\} = [K] \{F\} + \{C\}P + \{\Gamma\} \quad (2.21)$$

where:

- $\{w\}$ is the vector containing crack opening displacements;
- $[K]$ is the matrix containing the nodal displacements for a unit applied force;
- $\{F\}$ is the vector containing the nodal forces;
- $\{C\}$ is the vector containing crack displacements for a unit external load;
- P is the external load;
- $\{\Gamma\}$ is the vector containing the crack opening due specimen weight;

Assuming that the initial crack tip is positioned in the node k and that the cross section of the element is discretized by means of n nodes, at the first step the following conditions have to be taken into account:

$$F_i = 0 \quad i = 1, 2, \dots, (k - 1) \quad (2.22a)$$

$$w_i = 0 \quad i = k, (k + 1), \dots, n \quad (2.22b)$$

The eqn. 2.21 and eqn. 2.22 constitute an algebraical system of $2n$ equations and $2n$ unknown, i.e. n value of forces and n values of displacements. If the load P is known, the deflection δ of the system may be calculated as:

$$\delta = \{C_F\}^T \{F\} + D_P P + D_\gamma \quad (2.23)$$

being:

- $\{C_F\}$ the vector containing the displacements generated by unit nodal force;
- D_P the value of displacement generated by a unit value of the external load;
- D_γ is the external displacement generated by the weight of the specimen.

It is worth noticing that the matrix $[K]$, the vectors $\{C\}$, $\{\Gamma\}$, $\{C_F\}$ and the D_P , D_γ values are computed once for all by means of a FEM procedure and conveniently scaled according to the analyzed problem.

After the first step, a cohesive zone develops and, in the general case of fig. 2.8, it may be included between the node j and m . Hence, eqs. 2.22 are replaced by:

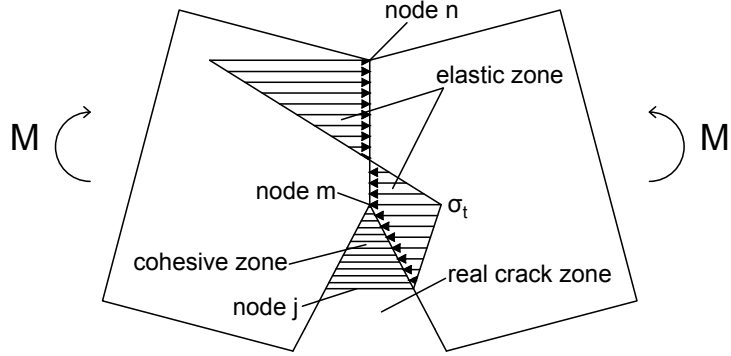


Figure 2.8: Generic situation for the algorithm

$$F_i = 0 \quad i = 1, 2, \dots, (j - 1) \quad (2.24a)$$

$$F_i = F_t \left(1 - \frac{w_i}{w_{cr}^t} \right) \quad i = j, (j + 1), \dots, m \quad (2.24b)$$

$$w_i = 0 \quad i = m, (m + 1), \dots, n \quad (2.24c)$$

where F_t is the ultimate nodal tensile strength and is calculated as:

$$F_t = \frac{b \cdot \sigma_t}{n - 1} \quad (2.25)$$

At the first step, the cohesive zone is missing and the load P_1 that is able to generate the ultimate tensile nodal force F_t in the node k is computed. Thus, by means of eqn. 2.23 it is possible to calculate δ_1 . The couple (δ_1, P_1) constitute the first point of the load-deflection curve. At the end of the first step, the fictitious tip is moved in the node $(k + 1)$ and the cohesive zone extends between the node k and $(k + 1)$. Hence, the value of the load P_2 that is able to generate the ultimate force F_t in the node $(k + 1)$ is computed and applying eqn. 2.23, 2.21, 2.24, nodal displacement $\{w\}$, nodal forces $\{F\}$ and deflection δ_2 are computed. The couple (δ_2, P_2) constitute the second point of the load-deflection diagram. At the third step, the fictitious tip is moved forward, and so on.

The numerical procedure stops when the fictitious tip reaches the node n and all the other nodes of the middle cross section get untied. Furthermore, it is worth

noticing that in each step a control is made on the $\{w\}$ displacement solution in order to calculate the position of the real crack tip.

In fig: 2.9, fig:2.10, fig:2.11 (σ_u is the ultimate tensile strength in the original notation of the author) are reported the numerical investigations carried out by Carpinteri for plain concrete members [33, 34] having the energy brittleness numbers s_E reported in tab. 2.1 and for initial notch dimension: $a_0/b = 0.1, 0.3, 0.5$ respectively.

$A : s_E = 2.09 \cdot 10^{-5}$	$E : s_E = 10.45 \cdot 10^{-5}$	$I : s_E = 83.59 \cdot 10^{-5}$	$O : s_E = 6.27 \cdot 10^{-3}$
$B : s_E = 4.18 \cdot 10^{-5}$	$F : s_E = 20.90 \cdot 10^{-5}$	$L : s_E = 1.04 \cdot 10^{-3}$	$P : s_E = 8.36 \cdot 10^{-3}$
$C : s_E = 6.27 \cdot 10^{-5}$	$G : s_E = 41.80 \cdot 10^{-5}$	$M : s_E = 2.08 \cdot 10^{-3}$	$Q : s_E = 10.45 \cdot 10^{-3}$
$D : s_E = 8.36 \cdot 10^{-5}$	$H : s_E = 62.70 \cdot 10^{-5}$	$N : s_E = 4.18 \cdot 10^{-3}$	$R : s_E = 20.90 \cdot 10^{-3}$

Table 2.1: Energy brittleness number s_E investigated by Carpinteri

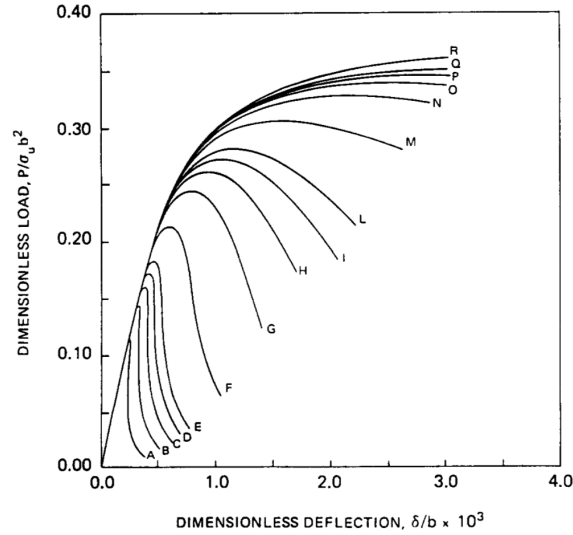


Figure 2.9: Dimensionless load vs. deflection diagrams by varying the brittleness number s_E ($\lambda = 4, a_0/b = 0.1, \varepsilon_t = 0.87 \cdot 10^{-4}$)

It may be seen that for low s_E numbers, i.e. high tensile strength and high beam depth, a snap-back branch is revealed. More precisely, for $s_E \leq 8.36 \cdot 10^{-5}$ a catastrophic branch with a positive slope is obtained (fig. 2.9). Moreover, comparing the three diagrams, it may be seen that increasing the dimension of the initial notch, albeit a lower maximum load is achieved, the post-peak branches exhibit a more stable behavior.

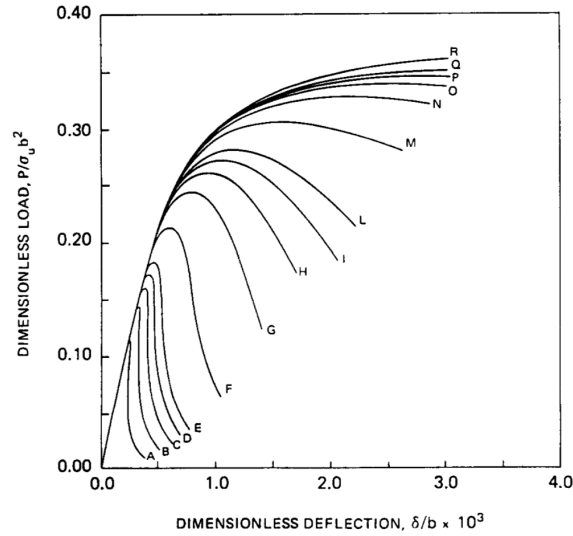


Figure 2.10: Dimensionless load vs. deflection diagrams by varying the brittleness number s_E ($\lambda = 4$, $a_o/b = 0.3$, $\varepsilon_t = 0.87 \cdot 10^{-4}$)

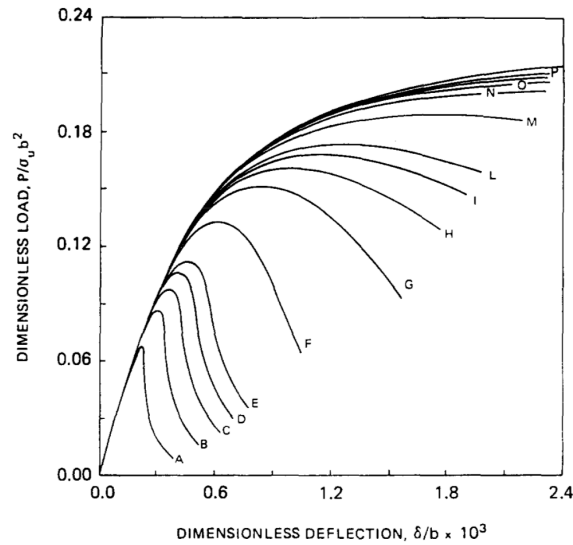


Figure 2.11: Dimensionless load vs. deflection diagrams by varying the brittleness number s_E ($\lambda = 4$, $a_o/b = 0.5$, $\varepsilon_t = 0.87 \cdot 10^{-4}$)

2.5 Smeared tip algorithm

The smeared tip algorithm has been proposed by Planas et al. [35, 36] and improved by Břzant [37, 38] and Břzant et al. [39]. It is based on the superposition of LEFM cases carrying to triangular systems of equations that may be solved by means of

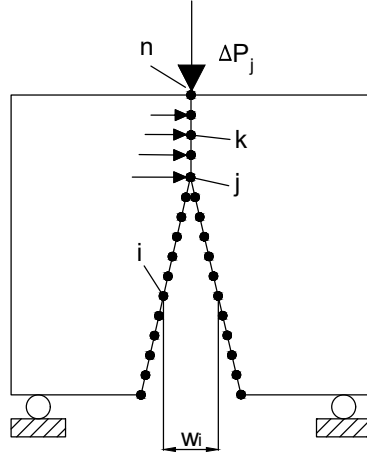


Figure 2.12: Basic linear elastic case for the smeared-tip superposition

a forward substitution. In each case a stress free cracked beam portion having the tip in the node j ($j = 1, 2, \dots, n - 1$) and subjected to the load ΔP_j is considered as depicted in fig. 2.12. Hence, the forces F_i , crack openings w_i and the external load P are written as:

$$F_i = \sum_{j=1}^{(n-1)} R_{ij} \Delta P_j \quad (2.26)$$

$$w_i = \sum_{j=1}^{(n-1)} D_{ij} \Delta P_j \quad (2.27)$$

$$P = \sum_{j=1}^{(n-1)} \Delta P_j \quad (2.28)$$

where:

- R_{ij} is the force at the node i generated by a unit external load when the tip of the crack is positioned in the node j ;
- D_{ij} is the crack opening at the node i generated by a unit external load when the tip of the crack is positioned in the node j .

Since the crack faces are in a stress free condition, the R_{ij} and D_{ij} may be stored

in triangular matrices:

$$R = \begin{bmatrix} R_{11} & 0 & 0 & \dots & 0 \\ R_{21} & R_{22} & 0 & \dots & 0 \\ \vdots & \vdots & \vdots & \vdots & \vdots \\ R_{(n-2)1} & R_{(n-2)2} & \dots & R_{(n-2)(n-2)} & 0 \\ R_{(n-1)1} & R_{(n-1)2} & \dots & R_{(n-1)(n-1)} & R_{(n-1)(n-1)} \end{bmatrix} \quad (2.29)$$

$$D = \begin{bmatrix} 0 & D_{12} & D_{22} & \dots & D_{1(n-1)} \\ 0 & 0 & D_{23} & \dots & D_{2(n-1)} \\ \vdots & \vdots & \vdots & \vdots & \vdots \\ 0 & 0 & \dots & 0 & D_{(n-2)(n-1)} \\ 0 & 0 & \dots & 0 & 0 \end{bmatrix} \quad (2.30)$$

In order to compute $[R]$ and $[D]$, it is necessary to perform $(n-1)$ analysis through a FEM program simulating the central beam part having a crack tip in the node $1, 2, \dots, (n-1)$.

Hence, assuming a generic cohesive zone between the nodes p and m and a softening law $F = f(w)$, it is possible to write:

$$\sum_{j=1}^i R_{ij} \Delta P_j = 0 \quad i = 1, 2, \dots, c-1 \quad (2.31a)$$

$$\sum_{j=1}^i R_{ij} \Delta P_j = f \left(\sum_{j=i+1}^{(n-1)} D_{ij} \Delta P_j \right) \quad i = c, \dots, m \quad (2.31b)$$

$$\sum_{j=1}^i D_{ij} \Delta P_j = 0 \quad i = (m+1), \dots, (n-1) \quad (2.31c)$$

The eqn. 2.31a and 2.31c give immediately

$$\Delta P_j = 0 \quad j \neq c, \dots, m \quad (2.32)$$

Thus, the problem is reduced to the solution of the non-linear system composed

by $(m - c + 1)$ equations:

$$\sum_{j=c}^i R_{ij} \Delta P_j = f \left(\sum_{j=i+1}^m D_{ij} \Delta P_j \right) \quad i = c, \dots, m \quad (2.33)$$

The eqn. 2.33 may be solved iteratively and once the difference between a computation step and the previous one is lower than a prefixed tolerance, the crack faces forces, the crack openings and the external load may be computed through eqns. 2.26 - 2.28

Chapter 3

The crushing failure

The most used constitutive law for concrete in compression, e.g. the parabolic-perfectly plastic, the elastic-perfectly plastic and the Sargin's parabola, are defined in a *stress-strain* plane and are not able to take into account the size effects considering energy dissipation only over a volumetric domain. However, the size-effect in compression has been demonstrated widely in literature and has important consequences on the design of structures [40, 41]. Indeed, the compressive behavior of the material is evaluated by means of laboratory tests on specimens that may have a different scale order of magnitude compared to the real structures and hence, a different behavior. The strain localization in compression has been observed in the softening post peak branch [42] similarly to tensile softening. Hence, the introduction of constitutive laws that takes into account of the energy dissipation over an area rather than a volumetric domain may be able to predict the real behavior of the material [43–45]. In this chapter, the pioneering work of Hillerborg who constitute a first attempt to evaluate size-effect for concrete in compression is introduced. Hence, the overlapping crack model proposed by Carpinteri et al. [46–48] is treated and the parameters that constitute this model are widely explained.

3.1 The Hillerborg model

A first model for the compressive failure of concrete has been formulated by Hillerborg [49] for reinforced concrete beams, moving from the classical bending theory, to study the rotational capacity of these structures. Indeed, the main hypothesis

of his model are:

- plane sections remain plane after the deformation;
- the tensile strength of the material is completely neglected.

Hence, in order to explain energy dissipation, he introduced a strain localization zone having a width:

$$h = \eta x \tag{3.1}$$

where x is the depth of the neutral axis of the section and η is a coefficient that may be determined by means of experimental tests (however, its mean value is 0.8). The softening law in compression is defined in the plane $\sigma - w^c$ and has a slope depending on the depth of the section. Thus, assuming the classical stress - strain relationships for steel and the elastic-softening law aforementioned for concrete in compression, Hillerborg was able to calculate the moment-curvature diagrams as is commonly done in reinforced concrete structures theory. The essential difference from the classical moment-curvature diagrams is that the Hillerborg ones are size dependent since the constitute law adopted is defined by means of section depth.

The model proposed by Hillerborg is quite rough but represented a first attempt to take into account of size-effects for concrete in bending.

3.2 The overlapping model

The overlapping model has been introduced by Carpinteri et al. [46–48] in order to simulate the damage of concrete in compression, i.e. *crushing*. It is formally comparable to the cohesive model and indeed, the damage process is performed through an interpenetration zone growing during the loading process. When the model is adopted, the following assumptions are made:

- the overlapping zone develops at one point of the specimen when the second principal stress reaches the compressive strength σ_c ;
- the crushing zone grows perpendicular to the second principal stress;
- the overlapping zone is divided into two parts. The zone where the material, albeit damaged, is still able to transfer stresses constitutes the process compressive zone and for this region an overlapping law defined in the plane

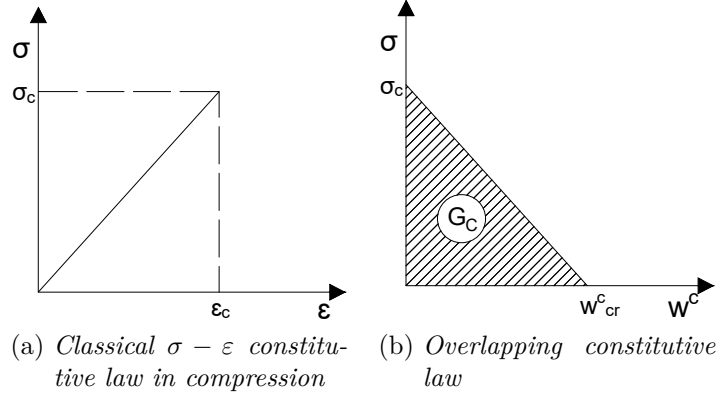


Figure 3.1: Couple of constitutive laws adopted for undamaged (a) and damaged material (b) in compression

$\sigma - w_{cr}^c$ is adopted (fig. 3.1b). Meanwhile, the zone on the rear point where the interpenetration reaches the threshold width w_{cr}^c , constitutes the stress free area of the crushing zone.

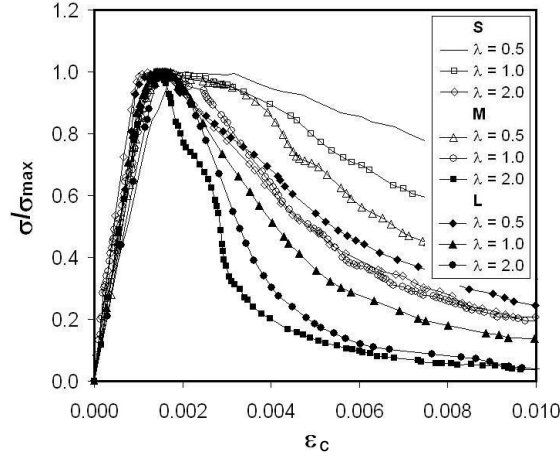
- the material outside the overlapping zone is assumed to be in the elastic field and a classical $\sigma - \varepsilon$ law is adopted (fig. 3.1a).

In the present work a linear overlapping law is adopted, although more complicated shapes could be used:

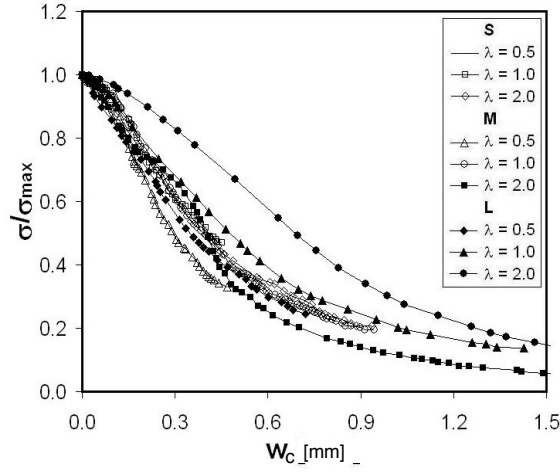
$$\sigma = \sigma_c \left(1 - \frac{w^c}{w_{cr}^c} \right) \quad (3.2)$$

The area below the $\sigma - w^c$ curve defines the crushing energy G_C and, it may be considered a true material parameter if the specimen is quite large [50].

In order to validate this assumption, the experimental compression tests taken by Ferrara and Gobbi [45] may be considered. They analyzed specimens varying both slenderness λ from 0.5 to 2, and scales (1,2,4). The non-dimensional loading curves obtained by the tests are depicted in fig. 3.2a where S, L, M identify three different dimension classes. It may be seen that the elastic branch is independent by the size of the specimen and, indeed, the slope is only a function of the elastic modulus of the material. Nevertheless, the post-peak is widely affected by the size and, indeed the curves are quite scattered which imply that a stress-strain law may not be assumed as a material property when the maximum load is overcome. On the other hand, it is possible to take into account of the interpenetration w^c of the



(a) $\sigma - \varepsilon_c$ relationship



(b) $\sigma - w^c$ post-peak relationship

Figure 3.2: Uniaxial compression test on specimens with different dimension and slenderness. S , M , L , denote respectively, small, medium and large specimen

material in the softening regime.

The material overlapping is calculated subtracting the elastic expansion generated by the reduction of the stress to the shortening of the specimen.

In fig. 3.2b the dimensionless load is plotted against w^c and it may be seen that the several curves are restricted within a limited zone demonstrating that a $\sigma - w^c$ law may be assumed as a real constitutive law of the material. The experimental results obtained by Ferrara and Gobbi have been confirmed by several authors [50,

51] allowing to assume the compressive dissipated energy G_C as a real material parameter.

Suzuki et al. [52] have proposed an empirical equation, obtained through compression tests carried on both plain and transverse reinforced concrete specimens, that is able to compute the crushing energy taking into account the concrete confined compressive strength, stirrups yielding stress and stirrups volumetric content:

$$G_C = G_{C,0} + 10000 \frac{k_a^2 p_e}{\sigma_c} \quad (3.3)$$

where σ_c is the average concrete compression strength and $G_{C,0}$ is the crushing energy for unconfined concrete:

$$G_{C,0} = 80 - 50k_b \quad (3.4)$$

k_a depends on stirrups strength and volumetric percentage:

$$k_a = 1 + k_e \frac{f_{sy} - f_{s,c}}{f_{sy}} \quad (3.5)$$

and p_e is the effective lateral pressure:

$$p_e = k_e \rho_w f_{s,c} \quad (3.6)$$

the parameter k_b depends on concrete strength σ_c :

$$k_b = \frac{40}{\sigma_c} \leq 1.0 \quad (3.7)$$

$f_{s,c}$ is the stress in the transverse reinforcement at the peak strength:

$$f_{s,c} = E_s \left[0.45 \varepsilon_{c0} + 6.8 \left(\frac{k_e \rho_w}{\sigma_c} \right)^{9/10} \right] \leq f_{sy} \quad (3.8)$$

k_e is the effective confinement coefficient:

$$k_e = \left(1 - \sum \frac{(w'_i)^2}{6b_c d_c} \right) \left(1 - \frac{s'}{2b_c} \right) \left(1 - \frac{s'}{2d_c} \right) / (1 - \rho_{cc}) \quad (3.9)$$

The units of measure in eqn. 3.3 - 3.9 are N and mm .

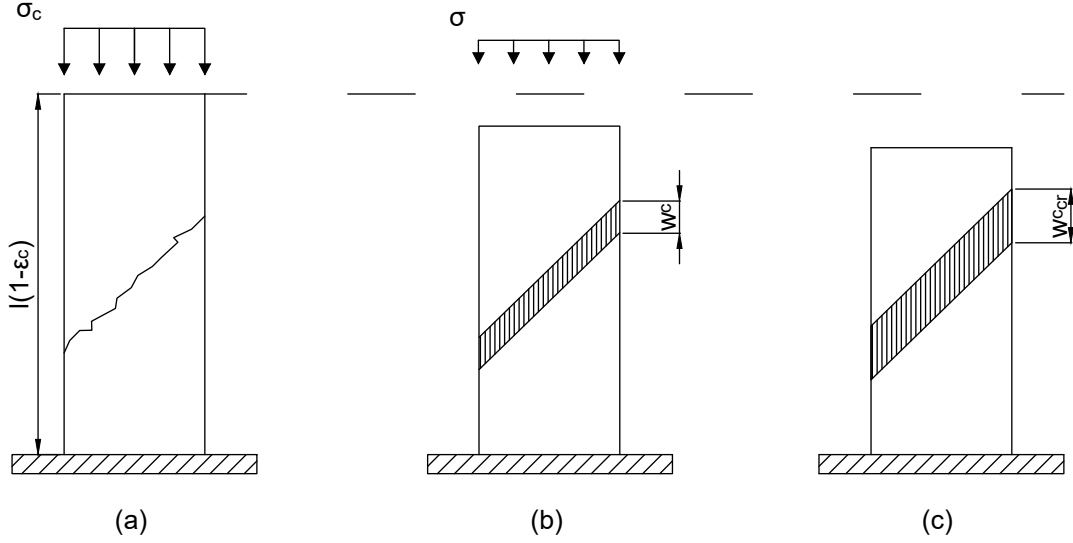


Figure 3.3: Stages of loading process of a specimen in compression

Furthermore, ρ_w is the geometric ratio of transverse reinforcement, E_s is the modulus of elasticity of transverse steel, $\varepsilon_{c0} = (0.0028 - 0.0008k_b)$, f_{sy} is the steel yielding strength, w'_i is the spacing between longitudinal bars, s' is the spacing between transverse reinforcement, b_c and d_c are the dimensions of the compressed concrete area whereas ρ_{cc} is the longitudinal compressed steel percentage.

Using Suzuki formula and varying the concrete compressive strength between 20 and 90 MPa, it is possible to observe that G_C ranges from 30 to 58 N/mm. Hence, G_C is bigger than G_F of 2-3 orders of magnitude, meanwhile, $w_{cr}^c \approx 1$ mm that is one order of magnitude higher than w_{cr}^t .

3.3 Uniaxial compression test of a specimen

The behavior of a plain concrete specimen subjected to uniaxial compression test may be characterized by three different stages as done for the slab subjected to a tensile test reported in the section 2.2.

Hence, referring to fig. 3.3 it is possible to observe that:

- In a first step, the specimen is within the elastic field and the displacement of

the upper edge may be calculated as:

$$\delta = \frac{\sigma}{E}l \quad \varepsilon \leq \varepsilon_c \quad (3.10)$$

- Once the ultimate resistance strength σ_c is achieved, a crushing band starts to develop as depicted in (a). In this phase, the material outside the damaged band has still an elastic behavior and, hence, the displacement of the upper side may be calculated as the sum of the specimen shortening and of the interpenetration displacement:

$$\delta = \frac{\sigma}{E}l + w^c \quad \varepsilon \leq \varepsilon_c \quad (3.11)$$

Taking into account of eqn. 3.2, it is possible to rewrite the eqn. 3.11 as

$$\delta = \frac{\sigma}{E}l + w_{cr}^c \left(1 - \frac{\sigma}{\sigma_c}\right) \quad w^c \leq w_{cr}^c \quad (3.12)$$

In this phase, the elastic zone expands while the stress decrease. Hence, the loading process may be carried in a stable manner only if the displacement control technique is used (however, a more severe unstable phenomena may occurs);

- In the stage (c), the strain concentration zone is heavily damaged and it is no longer able to transfer stresses:

$$\delta = 0 \quad \delta \geq w_{cr}^c \quad (3.13)$$

It is possible to rearrange eqn. 3.12 obtaining:

$$\delta = w_{cr}^c + \sigma \left(\frac{l}{E} - \frac{w_{cr}^c}{\sigma_c} \right) \quad (3.14)$$

The eqn. 3.14 inside a plane $\delta - \sigma$ represent a straight line with a slope depending on the sign of the term:

$$\frac{l}{E} - \frac{w_{cr}^c}{\sigma_c} \quad (3.15)$$

Hence, softening occurs when:

$$\frac{l}{E} - \frac{w_{cr}^c}{\sigma_c} < 0 \quad (3.16)$$

on the other hand, a snap-back post-peak branch is described when:

$$\frac{l}{E} - \frac{w_{cr}^c}{\sigma_c} \geq 0 \quad (3.17)$$

which may be expressed as:

$$\frac{w_{cr}^c/2b}{\varepsilon_c \lambda} \leq \frac{1}{2} \quad (3.18)$$

The ratio $w_{cr}^c/2b$ is the *energy brittleness number in compression* s_E^c . Hence, the eqn. 3.16 demonstrates that the brittleness of the specimen depends on the combination of low crushing energy, large scale and/or slenderness. Furthermore, the eqn. 3.18 has the same meaning of eqn. 2.5 defined for tensile tests and the graphs of fig. 2.4 may be consequently traced also in compression.

Chapter 4

The cohesive/ overlapping algorithm

This numerical algorithm has been proposed by Carpinteri et al. [22–28] and Corrado [29] and may be considered a development of the original numerical procedure recalled in section 2.4.

The numerical resolution is a step-by-step procedure in which the driving parameters are the positions of the cohesive fictitious crack tip and of the overlapping fictitious crack tip: starting from their initial positions, the tip that reaches the ultimate condition, corresponding to the achievement of the ultimate strength, is computed and only this tip is moved forward in the next step. At each step, resolution is governed by the equation:

$$\{w\} = [K_F]\{F\} + \{K_M\}M \quad (4.1)$$

being:

- $\{w\}$ the opening/ overlapping displacements vector;
- $[K_F]$ a matrix containing nodal displacements generated by a unit force;
- $\{F\}$ vector containing nodal forces;
- $[K_M]$ the matrix containing nodal displacements for a unit applied bending moment;

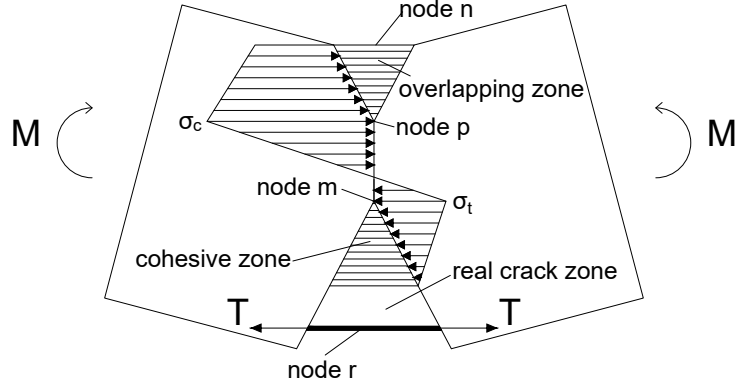


Figure 4.1: Forces distribution considered by the cohesive/ overlapping algorithm

- M value of the applied bending moment.

According to the cohesive and overlapping models, in the general case of fig. 4.1, it is necessary to take into account of the following conditions:

$$F_i = 0 \quad i = 1, 2, \dots, (j - 1), i \neq r \quad (4.2a)$$

$$F_i = F_t \left(1 - \frac{w_i}{w_{cr}^t} \right) \quad i = j, \dots, (m - 1) \quad (4.2b)$$

$$w_i = 0 \quad i = m, \dots, p \quad (4.2c)$$

$$F_i = F_c \left(1 - \frac{w_i}{w_{cr}^c} \right) \quad i = (p + 1), \dots, q \quad (4.2d)$$

$$F_i = 0 \quad i = (q + 1) \dots, n \quad (4.2e)$$

$$F_i = f(w_i) \quad i = r \quad (4.2f)$$

where:

- j : real cohesive crack tip;
- m : fictitious cohesive crack tip;
- p : fictitious overlapping crack tip;
- q : real overlapping crack tip;
- r : reinforcement node position.

The eqn. 4.2b and eqn. 4.2d represent the softening cohesive and overlapping laws, while the eqn. 4.2f is the equation that is able to relate the crack opening value with the reaction exerted by the reinforcement layer. This equation will be discussed in details at the end of this paragraph.

The eqn. 4.1 and 4.2 constitute a system of $2n$ equations and $(2n + 1)$ unknowns i.e. n displacements, n forces and the external load. In order to close the problem, it is necessary to calculate two potential value of M imposing the achievement of the ultimate strength in the two fictitious crack tips as aforementioned. The actual external load is fixed according to a minimum condition.

Hence, rotation is computed as

$$\vartheta = \{D_F\}^T \{F\} + D_M M \quad (4.3)$$

where:

- ϑ is the rotation of the analyzed beam portion;
- $\{D_F\}$ is the vector containing the rotation generated by unit nodal forces;
- D_M is the rotation generated by a unit applied bending moment;

The matrix $[K_F]$, the vectors $\{K_M\}$ $\{D_F\}$ and the D_M value, have been computed by means of the software FEAP [53] developed by the Berkeley University analyzing a beam portion having a length of 200 mm and a depth of $b = 400\text{ mm}$ as depicted in fig. 4.2.

As regarding steel, the classical $\sigma - \varepsilon$ constitutive law may not be used for the purpose of the program since the kinematical behavior of the mechanical system is described by means of crack openings. Hence, a law that is able to relate the force exerted by the reinforcement layer and the crack opening has been obtained by means of bond-slip considerations reported in Model Code 90 [32, 54–56]. Indeed, the bond stresses τ that exchange concrete and steel may be calculated as a function of the relative slip s :

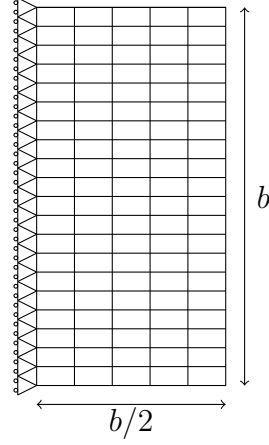


Figure 4.2: Numerical simulation scheme used to compute elastic coefficients of the algorithm

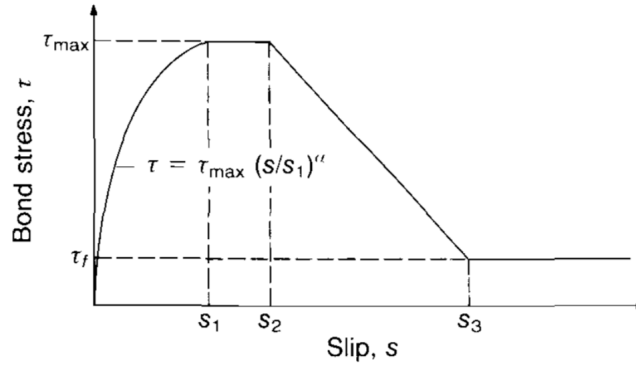


Figure 4.3: Bond-slip law assumed by MC90

$$\tau = \tau_{max} (s/s_1)^\alpha \quad 0 \leq s \leq s_1 \quad (4.4a)$$

$$\tau = \tau_{max} \quad s_1 < s \leq s_2 \quad (4.4b)$$

$$\tau = \tau_{max} - (\tau_{max} - \tau_f) \left(\frac{s - s_2}{s_3 - s_2} \right) \quad s_2 < s \leq s_3 \quad (4.4c)$$

$$\tau = \tau_1 \quad s > s_3 \quad (4.4d)$$

The eqns. 4.4 are represented in fig. 4.3. The values of $s_1, s_2, s_3, \alpha, \tau_{max}, \tau_f$

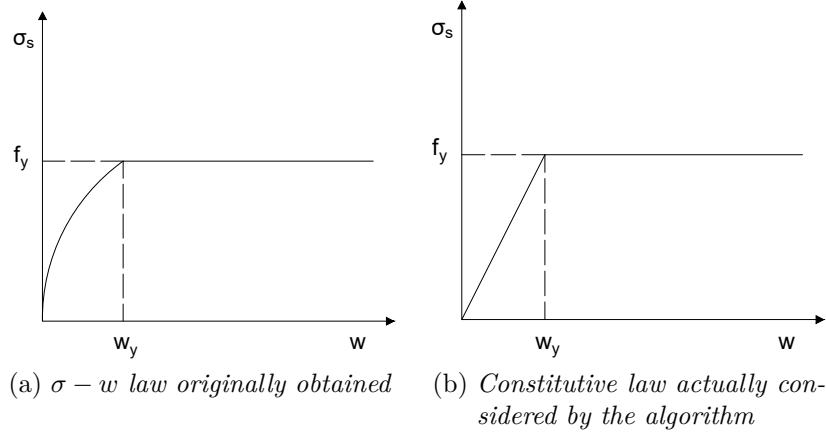


Figure 4.4: Constitutive laws of steel

depend on concrete confinement and bond conditions. In order to obtain a bond-slip relationship for reinforcement, the following calculation steps have been carried out [29]:

- It is assumed that the slip, in the section where the fracture is present, is equal to half the fracture width itself;
- It is assumed that the slip s may be described by a linear function over the transferring length L_τ i.e., length along which concrete and steel exchange stresses;
- According to the slip s law assumed in the aforementioned point, τ stresses are calculated by means of eqn. 4.2;
- Integrating τ along L_τ , the value T of the force exerted by the reinforcement layer is obtained. The value of this force depends on the value of the total slip assumed at the beginning of this procedure and, hence on the crack width.

Once the value of the crack width that is able to generate steel yielding w_y is gained, the force T is set equal to $T = f_y \cdot A_s$ for whichever value of the crack opening.

Hence, the typical curve for steel in fig. 4.4a has been obtained assuming $f_y = 430 \text{ MPa}$, $E_s = 210 \text{ GPa}$, $\phi = 16 \text{ mm}$, $L_\tau = 20\phi$, $\tau_{max} = 11 \text{ MPa}$, $\tau_f = 1.6 \text{ MPa}$, $s_1 = 0.6 \text{ mm}$, $s_2 = 0.6 \text{ mm}$, $s_3 = 1.0 \text{ mm}$, $\alpha = 0.4$. The application of the law reported in fig. 4.4a may be troublesome due non linearity of the first branch. Hence,

the simpler bi-linear law of fig. 4.4b is effectively considered inside the algorithm and the value of w_y is fixed to 0.4 mm .

Chapter 5

The new cohesive/ overlapping algorithm

In this part of the work, the new cohesive/ overlapping algorithm will be presented and its routines will be discussed in details.

The program has been written using Matlab ver. 2019a and keeps the original theoretical background of that presented by Carpinteri et al. albeit there are many differences, which will be outlined, referring to equations management and the evaluation of the effects of the reinforcement layer.

Furthermore, in order to test the applicability of the program also to pre-stressed concrete beams, an additional routine that is able to take into account of the presence of an axial force has been written.

5.1 The routine `GUI.mlapp`

The *GUI.mlapp* constitutes the user interface of the algorithm and, it is made of three different "faces": the first one is dedicated to the data input of the problem, the second one is able to show the results for each computation step, while in the third one $P - \delta$ or $M - \vartheta$ curves are plotted inside a dedicated environment.

In the first face (fig. 5.1), the user is able to decide if the analysis has to be done taking into account only the crack opening or both crack opening and concrete crushing. The choice is memorized inside the variable *crushing*. Furthermore, the user may choice also the initial notch tip and the value of a possible prestressing

The screenshot shows a software interface with the following sections:

- General input data:**
 - Number of nodes: 161 (dropdown)
 - Calculation with concrete crushing:
 - Presence of reinforcement:
 - Prestressing force:
 - Position node of the initial crack tip: 80 (input)
- Geometric and mechanic parameters:**
 - Base of the section [cm]: 40.00 (input)
 - Depth of the section [cm]: 80.00 (input)
 - Beam length [cm]: 320.00 (input)
 - Original Young modulus [Mpa]: 30000.00 (input)
- Cohesive laws parameters:**
 - Ultimate tensile strength in tension [MPa]: 4.00 (input)
 - Ultimate tensile strength in compression [MPa]: 40.0 (input)
 - Critic displacement value in tension [mm]: 0.040000 (input)
 - Critic displacement value in compression [mm]: 1.50000 (input)
- Output energy parameters:**
 - Fracture tension energy [Mpa·mm]: 0.0000 (input)
 - Fracture compression energy [Mpa·mm]: 0.0000 (input)
 - Brittleness number S_E [-]: 0 (input)
 - Brittleness number N_ϕ : 0 (input)
- Prestressing Table:**
 - Node: 40 (input)
 - Steel quantity [mmq]: 0.00 (input)
 - Prestressing force [kN]: 0.00 (input)
- Reinforcement table:** A table with columns: Node, Diameter [mm], N. bars [-].
- Calculate:** A central button.

Figure 5.1: User interface of the new algorithm

force which quantities are memorized inside $initipt$, Fp , respectively. In the central column it is possible to enter the mechanical properties of the concrete matrix such as tensile and compressive ultimate strengths and critic displacements w_{cr}^t and w_{cr}^c for cohesive and overlapping softening laws. The current version of the program is able to deal only with linear softening $\sigma - w$ curves and, hence the fracture energy G_F and the crushing energy G_C , that are showed as first outputs, are computed through the triangle area formula.

On the right part of the current face there is the reinforcement table in which the user may decide the node where to place a reinforcement layer, the nominal bars diameter and the number of bars. The reinforcement table has been created thinking of future developments of the algorithm and, although the GUI allow to insert more levels of reinforcement, the actual version of the program is able to manage only one bars layer. The information about reinforcement is memorized inside the matrix *data*.

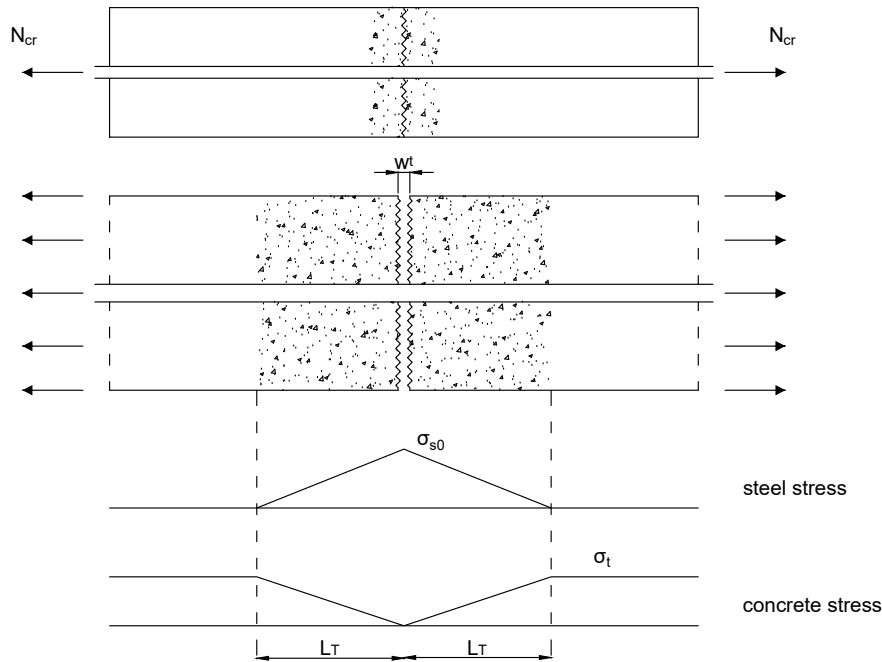


Figure 5.2: Steel-concrete interaction

```
[coer,fo,wy,IndexAs,...
thickness,Ast,I] = ReinforcementData(data,high,thickness,...
I,Es,E,fus,fo1,Fp,tau,nnod,pres)
```

Figure 5.3: Variables managed by ReinforcementData.m

5.2 The routine ReinforcementData.m

This routine is able to evaluate both the effect of a reinforcement layer and of a prestressed straight cable. As regarding classical reinforcement, a study on bond-slip relationship [57, 58] has been done. Indeed, the classical $\sigma - \varepsilon$ constitutive law usually adopted for steel cannot be used for the purpose of this work because the kinematic of the structural system is characterized by the crack opening w^t .

It is possible to consider a tensed member as depicted in fig. 5.2 and to apply an axial force N_{cr} generating the cracking of the middle cross section.

In correspondence of the fracture, the force is carried only by the steel layer while at a distance L_τ , the stress is equal to σ_t due τ stresses that exchange concrete and

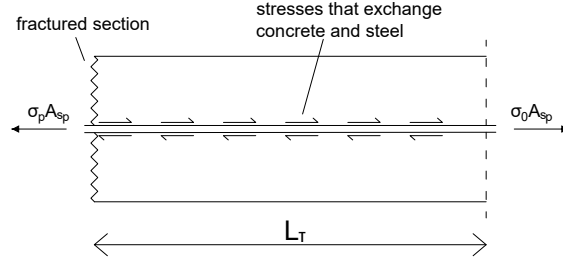


Figure 5.4: Pre-stressed steel-concrete interaction

steel. Hence, it is possible to find out L_τ writing the equilibrium equation:

$$\sigma_{s0} A_s = \int_0^{L_\tau} \pi \phi \tau(x) dx \quad (5.1)$$

Since the τ stresses variation description is quite complicated (for more details see [58]) it may be possible to assume an average value τ_m (the Model Code 2010 suggests to adopt $\tau_m = 1.8\sigma_t$) and the 5.1 may be rewrite as:

$$L_\tau = \frac{\sigma_{s0} A_s}{\pi \phi \tau_m} \quad (5.2)$$

Along L_τ the stress inside steel varies linearly (τ stresses have been assumed constant) from a maximum value σ_{s0} in correspondence of the fracture to a minimum one that may be assumed, for sake of simplicity, null. Therefore:

$$\sigma_s(x) = \sigma_{s0} \left(1 - \frac{x}{L_\tau} \right) \quad (5.3)$$

Fracture opening may be calculated as two times the integral of the strain difference between steel and concrete along L_τ . However, the deformation of concrete is negligible and taking into account of eqn. 5.2, 5.3 it is possible to obtain:

$$w^t = \frac{\sigma_{s0}^2 A_s}{E_s \pi \phi \tau_m} \quad (5.4)$$

In the case of a pre-stressed reinforcement layer, all the aforementioned considerations may be repeated.

It is possible to imagine a prestressed part of a beam of length L_τ at the first crack formation stage as depicted in fig. 5.4. Along the distance L_τ , concrete and steel exchange τ stresses and hence, imposing equilibrium it is possible to find out

the new expression of L_τ for pre-stressed members:

$$L_T = \frac{(\sigma_p - \sigma_{p0})A_{sp}}{\pi\phi\tau_m} \quad (5.5)$$

where $(\sigma_p - \sigma_{p0})A_{sp}$ represents the increasing of force inside steel due cracking. It is worth noticing that the eqn. 5.5 is equal to the formula provided in clause 7.4.3.2. by Model Code 90.

The crack width, due symmetry, is equal to twice the integral of the deformation difference between concrete and steel along L_τ . Nevertheless, the deformation of concrete may be neglected and, it is possible to write:

$$w^t = 2 \int_0^{L_T} [\varepsilon_s(x) - \varepsilon_c(x)] dx \approx \frac{(\sigma_p - \sigma_{p0})^2 A_{sp}}{E_s \pi \phi \tau_m} \quad (5.6)$$

The implementation of eqn. 5.4 and 5.6 may be quite troublesome and thus, these laws have been used only to calibrate simpler expressions. More precisely, the 5.4 and 5.6 have been used to calculate w_y and an elastic-perfectly plastic constitutive law in the plane $\sigma - w^t$, as the original algorithm, as been assumed. Furthermore, for sake of simplicity, the hardening branch of the prestressing steel has been neglected.

The information on the steel effect is memorized in the variable *coer* and is elaborated by the routine *coerNoPres.m* and the routine *coerPres.m* depending on the value assumed by the flag *pres* end hence, depending on the presence of a prestressing force. Furthermore, it is worth noticing that the effects of a reinforcement layer are evaluated on the homogenized section of the analyzed beam.

5.3 The routine *master.m*

```
[fs,ws,thetas,Ms,deltas,fos,ntipts,ntipats,ntipcs,...
ntipacs,nstep,inoda,Ast]=master(initipt,ft,fc,wct,wcc,...
data,span,thickness,...
high,E,I,crushing,rein,Fp,pres,nodes)
```

Figure 5.5: Variables managed by *master.m*

The function *master.m* is the main routine of the algorithm and it manages the calling of other routines and the handover of variables. Furthermore, it controls

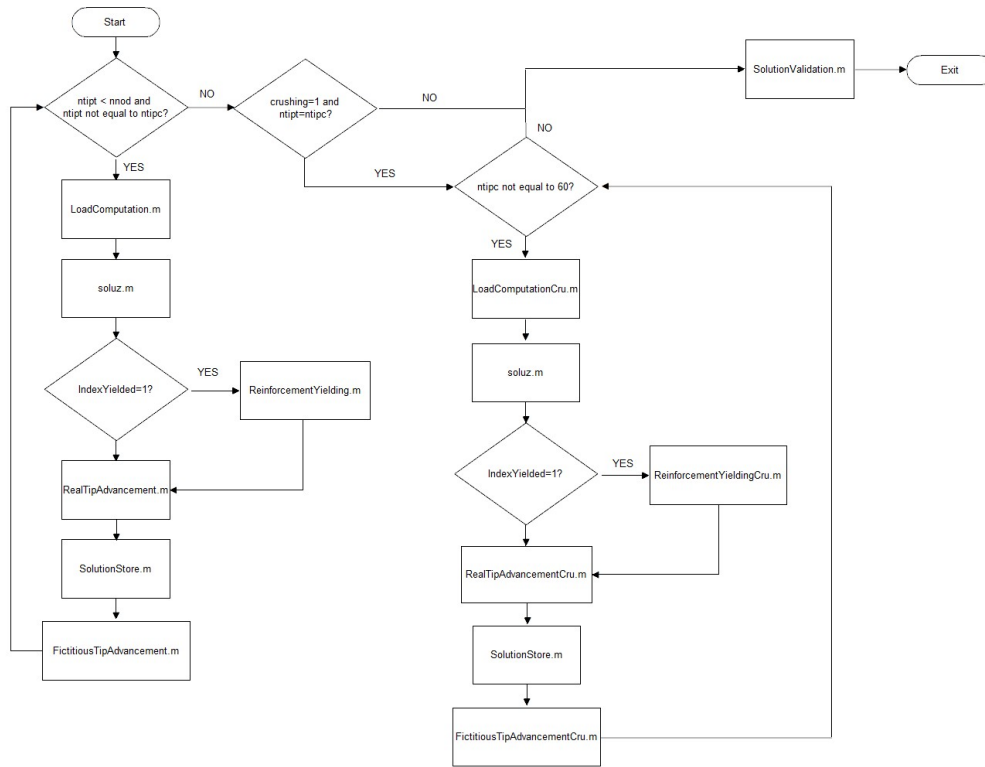


Figure 5.6: Function scheme of the routine *master.m*

the cycles that are made according to the desired analysis and indeed it is divided into two parts; the first one consists in a loop (always performed) that is able to move the tensed or compressed fictitious crack tip, while the second cycle is able to move the two tips towards the soffit of the beam. This last loop is done only if it is required to take into account of the concrete crushing and if the two tips meet themselves at the end of the previous loop.

In fig. 5.6 is depicted a flow chart showing the operations that are made by this routine and the other functions that are called.

5.4 The routine **LoadComputation.m**

This routine is able to calculate the external bending moment M generating the ultimate strength in the cohesive fictitious crack tip $ntipt$ or in the overlapping fictitious crack tip $ntipc$.

```
[M,cru,IndexYielded]=LoadComputation(ntipt,ntipat,ncort,...
ntipc,ntipac,ncorc,...
      M,fut,wct,fuc,wcc,nnod,...
      coe,coer,fo,c,dcoe,dc,wy,flag,crushing,rein,...
      IndexAs,IndexYielded,pres)
```

Figure 5.7: Variables managed by LoadComputation.m

The routine exploits the solution calculated in the previous step calculation and, hence, the behavior of the system due a unit increment of M is measured. Then, two values of ΔM that are able to generate the conditions aforementioned are computed and the actual value of M is fixed according to a minimum condition. This minimum condition is set in order to work with the absolute value of ΔM taking into account that in the post-peak branch a softening or a snap-back may occur. If the analysis is set to take into account of a reinforcement layer, a third value of ΔM that is able to generate steel yielding is considered.

5.5 The routine soluz.m

```
[f,w, theta,IndexYielded]=soluz(ntipt,ntipat,ncort,ntipc,ntipac,ncorc,...
      M,fut,wct,fuc,wcc, nnod,...
      coe,coer,fo,c,dcoe,dc,wy,flag,crushing,...
      rein,IndexAs,IndexYielded,pres)
```

Figure 5.8: Variables managed by soluz.m

The routine is able to build a linear system of the type $[a]\{x\} = \{b\}$ according to the positions of both cohesive and overlapping cracks tips. The unknowns involve both forces and displacements and hence, it is no longer necessary to perform loops in order to obtain $\{F\}$ and $\{w\}$ separately, as done by the original program. As a matter of fact, the algorithm is not set to work with the eqn. 3.17 but:

$$\{F\} = [K_w]\{w\} + \{K_M\}M \quad (5.7)$$

being:

- $[K_w]$ the matrix containing nodal reactions generated by a unit nodal force;

- $\{K_M\}$ the vector containing nodal reactions generated by a unit external bending moment.

Hence, the general following linear system is constructed:

$$\left[a \right] = \begin{bmatrix} \left[K_w \right]_{rr} & -\left[K_w \right]_{rt} \frac{w_{cr}^t}{F_u} & \left[0 \right] & -\left[K_w \right]_{rc} \frac{w_{cr}^c}{F_c} & \left[K_w \right]_{r0} \\ \left[K_w \right]_{tr} & -\left[K_w \right]_{tt} \frac{w_{cr}^t}{F_u} - \left[I \right] & \left[0 \right] & -\left[K_w \right]_{tc} \frac{w_{cr}^c}{F_c} & \left[K_w \right]_{t0} \\ \left[K_w \right]_{er} & -\left[K_w \right]_{et} \frac{w_{cr}^t}{F_u} & -\left[I \right] & -\left[K_w \right]_{ec} \frac{w_{cr}^c}{F_c} & \left[K_w \right]_{e0} \\ \left[K_w \right]_{cr} & -\left[K_w \right]_{ct} \frac{w_{cr}^t}{F_u} & \left[0 \right] & -\left[K_w \right]_{cc} \frac{w_{cr}^c}{F_c} - \left[I \right] & \left[K_w \right]_{c0} \\ \left[K_w \right]_{0r} & -\left[K_w \right]_{0t} \frac{w_{cr}^t}{F_u} & \left[0 \right] & -\left[K_w \right]_{0c} \frac{w_{cr}^c}{F_c} & \left[K_w \right]_{00} \end{bmatrix} \quad (5.8)$$

$$\left\{ x \right\} = \begin{bmatrix} \left\{ w \right\}_r \\ \left\{ F \right\}^t \\ \left\{ F \right\}_e \\ \left\{ F \right\}^c \\ \left\{ w \right\}_0 \end{bmatrix} \quad \left\{ b \right\} = \begin{bmatrix} \left[K_w \right]_{rt} \left\{ w_{cr}^t \right\} - \left[K_w \right]_{rc} \left\{ w_{cr}^c \right\} - \left[K_M \right]_r M \\ \left[K_w \right]_{tt} \left\{ w_{cr}^t \right\} - \left[K_w \right]_{tc} \left\{ w_{cr}^c \right\} - \left[K_M \right]_t M \\ \left[K_w \right]_{et} \left\{ w_{cr}^t \right\} - \left[K_w \right]_{ec} \left\{ w_{cr}^c \right\} - \left[K_M \right]_e M \\ \left[K_w \right]_{ct} \left\{ w_{cr}^t \right\} - \left[K_w \right]_{cc} \left\{ w_{cr}^c \right\} - \left[K_M \right]_c M \\ \left[K_w \right]_{0t} \left\{ w_{cr}^t \right\} - \left[K_w \right]_{0c} \left\{ w_{cr}^c \right\} - \left[K_M \right]_0 M \end{bmatrix} \quad (5.9)$$

Once $\{F\}^t$ and $\{F\}^c$ are calculated, the crack opening and the interpenetrations values in the process zones are computed by means of eqn. 4.2b and eqn. 4.2d.

If the numerical analysis is done for a reinforced or pre-stressed member the eqn. 5.8 and eqn. 5.9 are modified by the routine *SystemModRein.m*. The manipulation that has to be performed, depends on the crack zone in which the node r is positioned and on which branch of the elastic-perfectly plastic law has to be taken into account.

5.6 The routine *RealTipAdvancement.m*

```
[f,w,theta,ntipat,ntipac,ncort,ncorc,M,cru] = ...  
RealTipAdvancement(f,w,theta,...  
    ntipt,ntipat,ncort,ntipc,ntipac,ncorc,...  
    M,fut,wct,fuc,wcc, mnod,coe,coer,fo,c, dcoe,...  
    dc,flag,crushing,cru,rein,IndexAs,wy,IndexYielded,pres)
```

Figure 5.9: Variables managed by *RealTipAdvancement.m*

This routine is able to perform a control on the displacements solution calculated in the current cycle. More precisely, it is able to check the displacements in both cohesive and overlapping zones and if solutions overcame w_{cr}^t or w_{cr}^t , real tip positions are moved forward, the extension of the processes zones are recalculated and a new solution is computed.

The routine is composed by several cycles as the real cohesive crack tip and the real crushing crack tip are moved alternatively of a unit position according to the minimum load condition. At the end of each cycles, control functions are recalled in order to check the convergence of the solution just performed.

If controls are successful, the cycles are broken and the algorithm memorize the new results.

Chapter 6

New algorithm results

In this chapter some numerical investigation carried through the new cohesive/overlapping algorithm will be presented and numerical vs. experimental curves will be plotted in order to validate the new numerical procedure.

6.1 Numerical investigation

In fig. 6.1 some dimensionless load vs. deflection diagrams are reported [59] varying the energy brittleness numbers s_E of the specimens. More precisely, the s_E numbers considered in the simulations are the same of tab. 2.1. The curves are obtained for $E_c = 30000 \text{ MPa}$, $\nu = 0.1$, $\varepsilon_t = 0.87 \cdot 10^{-4}$, $t = b$ for two slenderness ratio λ : 4, 16. In order to recognize the role of the initial notch, two values of the ratio a_o/b have been considered: 0.0 and 0.5.

In fig. 6.1a, it may be seen that the mechanical system exhibits an unstable behavior for $s_E < 10.45 \cdot 10^{-5}$ and, hence, a snap-back post-peak branch is traced. On the other hand, for curves $F - R$ the slope in the softening regime appear to be more and more stable as s_E becomes bigger. In fig. 6.1b the same geometry of fig. 6.1a are considered but an initial notch equal to one half of beams depths have been set in the numerical simulations. It may be worked out that, however this initial damage reduces the peak load for all the specimens, it changes the shape of the curve and, indeed, no snap-back is described even for low s_E numbers.

In fig. 6.1c, a slenderness ratio equal to 16 has been considered and a general embrittlement for all the specimens may be pointed out and, indeed, the curves

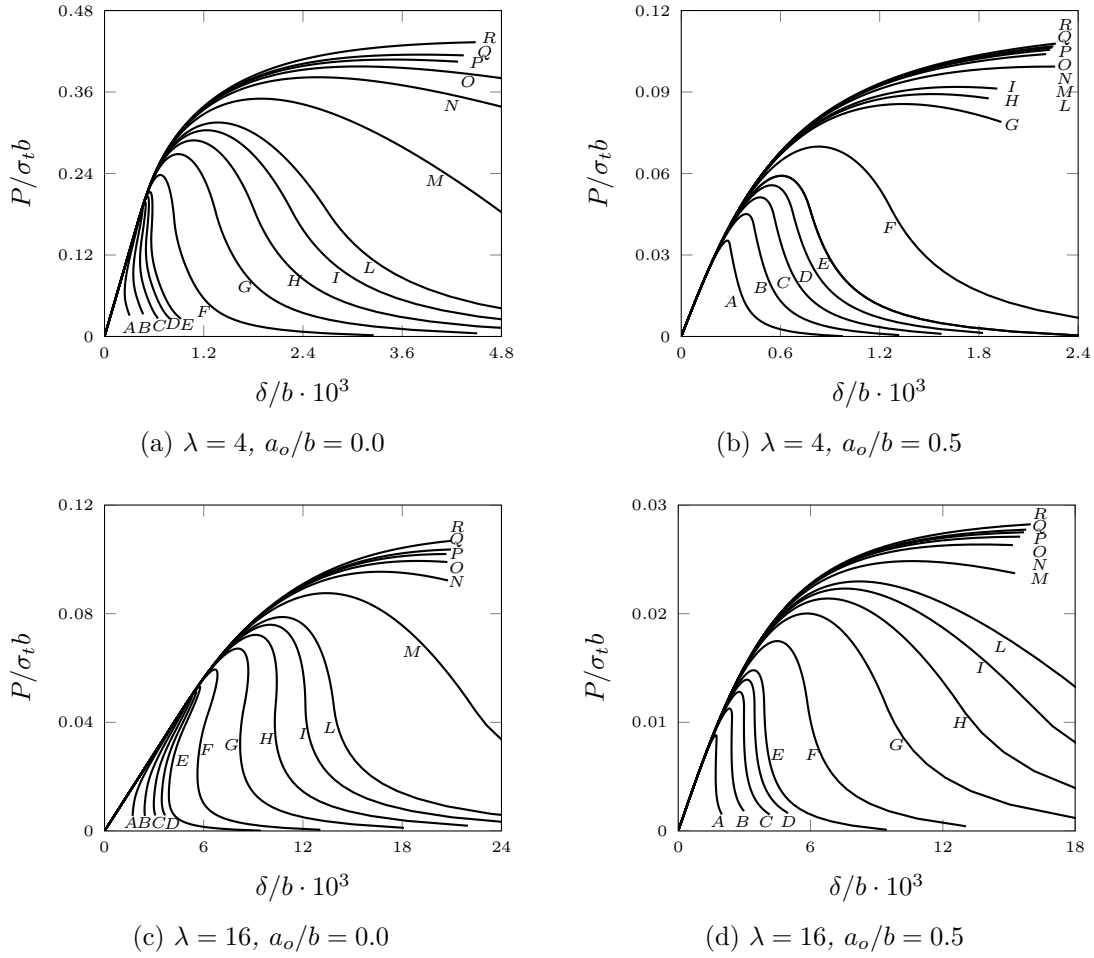
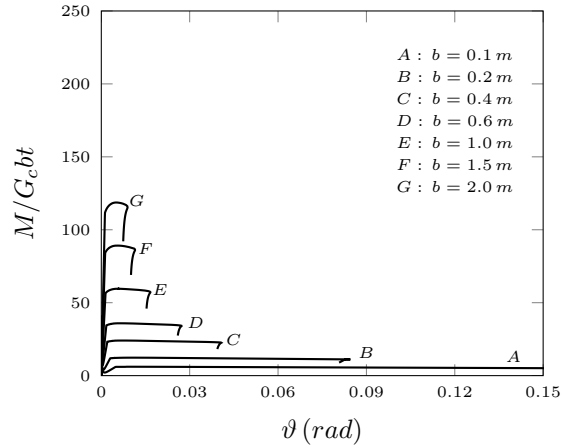


Figure 6.1: Dimensionless load vs. deflection diagrams of plain concrete beams for different geometries, crack lengths and s_E numbers

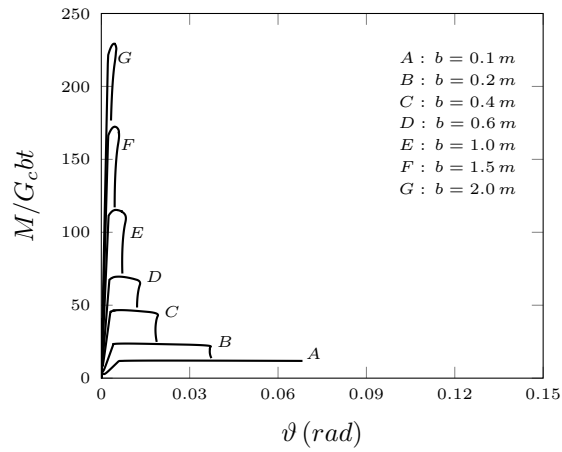
$A - D$ present a severe instability.

As referring to fig. 6.1c and fig. 6.1d, what have been indicated for fig. 6.1a and fig. 6.1b may be repeated.

In fig. 6.2 a numerical investigation carried on reinforced beams varying the depth b is presented. The results have been obtained assuming the following mechanical parameters: $\sigma_t = 4 \text{ MPa}$, $G_F = 0.08 \text{ N/mm}$, $\sigma_c = 40 \text{ MPa}$, $G_C = 30 \text{ N/mm}$. The yielding stress σ_y for steel has been assumed equal to 400 MPa and the d/b ratio has been fixed to 0.9 for all the specimens. In order to investigate size-effects the depths of the beams have been varied between 0.1 m and 2.0 m and two different



(a) Steel percentage: $\rho = 0.5\%$



(b) Steel percentage $\rho = 1.0\%$

Figure 6.2: Dimensionless load vs. rotation diagrams for different geometries and reinforcement ratio

steel percentage have been taken into account.

It may be seen in fig. 6.2a, that the ductility exploited by the mechanical system is inversely proportional to its own size: the beam having a depth equal to 0.1 m presents a high rotational capacity (for the definition of rotational capacity see fig. 8.1) while the beam with $b = 2.0\text{ m}$ shows a minimum plasticity resources. At the same time, for large beam depths, the crushing failure of concrete assume a more important role while, for small scale this phenomenon is neglectable. Hence, it is possible to assume that keeping the reinforcement ratio ρ constant, the behavior of the system is more unstable for large b .

In fig. 6.2b, it is possible to appreciate a general reduction on the plasticity resources of the mechanical systems albeit higher peak-loads are reached. The beam having $b = 2.0\text{ m}$ presents the most severe response and, indeed, once the maximum load is gained an almost vertical dropping occurs due unstable overlapping crack propagation.

6.2 Parametric analysis and experimental comparison

The experimental tests herein proposed, have been carried out by Carpinteri et al. [60] at the Department of Structural Engineering and Geotechnics of the Politecnico di Torino in order to investigate the size effects and the transition between failure mechanisms. Hence, specimens were prepared varying section depth b , slenderness ratio λ and steel percentage ρ .

Originally, 45 beams were casted however due laboratory movements, 10 beams cracked and consequently only 35 beams have been really tested. Beams were collected and labelled in three different classes according to cross sectional dimensions: (A) $100 \times 100\text{ mm}$, (B) $100 \times 200\text{ mm}$, (C) $200 \times 400\text{ mm}$. The slenderness ratio λ considered were $\lambda = 6, 12, 18$ and the effective depth to total depth ratio d/b has been fixed for all the specimens to 0.9.

The geometric and reinforced parameters of the tested specimens are reported in tab. 6.1.

In order to follow the tests in a stable manner, a closed-loop servo-controlled machinery has been adopted; the loading has been applied by means of displacements control for beams having a steel percentage larger than 0.50% while for the others the crack mouth opening displacement (CMOD) has been used. The test layout and machinery is reported in fig. 6.3.

The used steel bars had a diameters of 5, 8, 16, 20 mm having a yielding stress equal to 604, 643, 518, 567 MPa respectively. The average value of concrete compression strength f_{cm} has been assumed equal to 48.2 N/mm^2 and has been determined by means of eight cubic specimens. On the other hand, the elastic modulus of concrete has been determined on four specimens of $100 \times 100 \times 300\text{ mm}$ and a mean value of 35000 MPa has been assumed. The fracture energy G_F had been measured

Beam	Tension reinforcement	$A_s/(tb)$	N_P
A012-06	1 ϕ 5	0.20%	0.187
A025-06	2 ϕ 5	0.39%	0.374
A100-06	2 ϕ 8	1.00%	1.019
A200-06	4 ϕ 8	2.00%	2.038
A012-12	1 ϕ 5	0.20%	0.187
A025-12	2 ϕ 5	0.39%	0.374
A050-12	1 ϕ 8	0.50%	0.510
A100-12	2 ϕ 8	1.00%	1.019
A200-12	4 ϕ 8	2.00%	2.038
A025-18	2 ϕ 5	0.39%	0.374
A050-18	1 ϕ 8	0.50%	0.510
A100-18	2 ϕ 8	1.00%	1.019
A200-18	4 ϕ 8	2.00%	2.381
B012-06	2 ϕ 5	0.20%	0.265
B025-06	1 ϕ 8	0.25%	0.360
B050-06	2 ϕ 8	0.50%	0.721
B100-06	4 ϕ 8	1.00%	1.441
B200-06	2 ϕ 16	2.00%	2.322
B025-12	1 ϕ 8	0.25%	0.360
B100-12	4 ϕ 8	1.00%	1.441
B200-12	2 ϕ 16	2.00%	2.322
C012-06	2 ϕ 8	0.12%	0.255
C025-06	4 ϕ 8	0.25%	0.510
C050-06	2 ϕ 16	0.50%	0.821
C100-06	4 ϕ 16	1.00%	1.642
C200-06	4 ϕ 20	2.00%	2.810
C012-12	2 ϕ 8	0.12%	0.255
C100-12	4 ϕ 16	1.00%	1.642
C200-12	4 ϕ 20	2.00%	2.810
C012-18	2 ϕ 8	0.12%	0.255
C050-18	2 ϕ 16	0.50%	0.821
C100-18	4 ϕ 16	1.00%	1.642
C200-18	4 ϕ 20	2.00%	2.810

Table 6.1: Geometrical characteristics and steel percentages of tested beams

according to the RILEM recommendation [61] on six specimens and a mean value $G_F = 0.115 N/mm$ has been obtained. Hence, the stress intensity factor has been fixed to $K_{IC} = \sqrt{G_F E_c} = 63.4 Nmm^{-3/2}$.

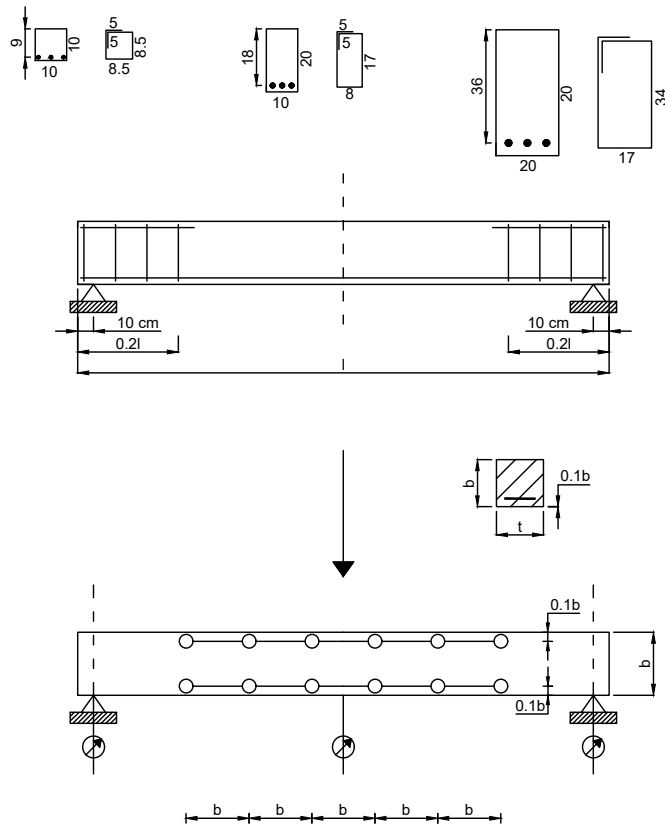


Figure 6.3: Test machinery adopted by Carpinteri et al.

From fig. 6.4 to fig. 6.11 a numerical vs. experimental comparison is made. Generally, it is possible to observe a good agreement of the numerical prediction with the experimental behavior proving the program to be capable of grasp the snap-back due concrete cracking, the steel yielding and the concrete crushing effectively. More precisely, for low steel percentage, the steel yielding precedes the concrete failure in compression and, hence, large plateau are described while for high steel amount, the plateau wide is strongly reduced due concrete crushing. The bigger differences between numerical and experimental results are outlined for high steel percentages; for these cases, indeed, the hypothesis of damage concentration in the middle cross section of the beam is quite unrealistic since it is more spread along beam length.

Nevertheless, the diagrams highlight a clear variation in failure mechanisms according to reinforcement area A_s , span and scale:

- Increasing the reinforcement area A_s and keeping the other parameters constant, there is a change from a flexural failure to a crushing one;
- Increasing the span and keeping the other parameters constant, there is a change from a compressive failure of concrete to a flexural one;
- Increasing the scale and keeping A_s constant there is a variation from a crushing failure to a flexural one.

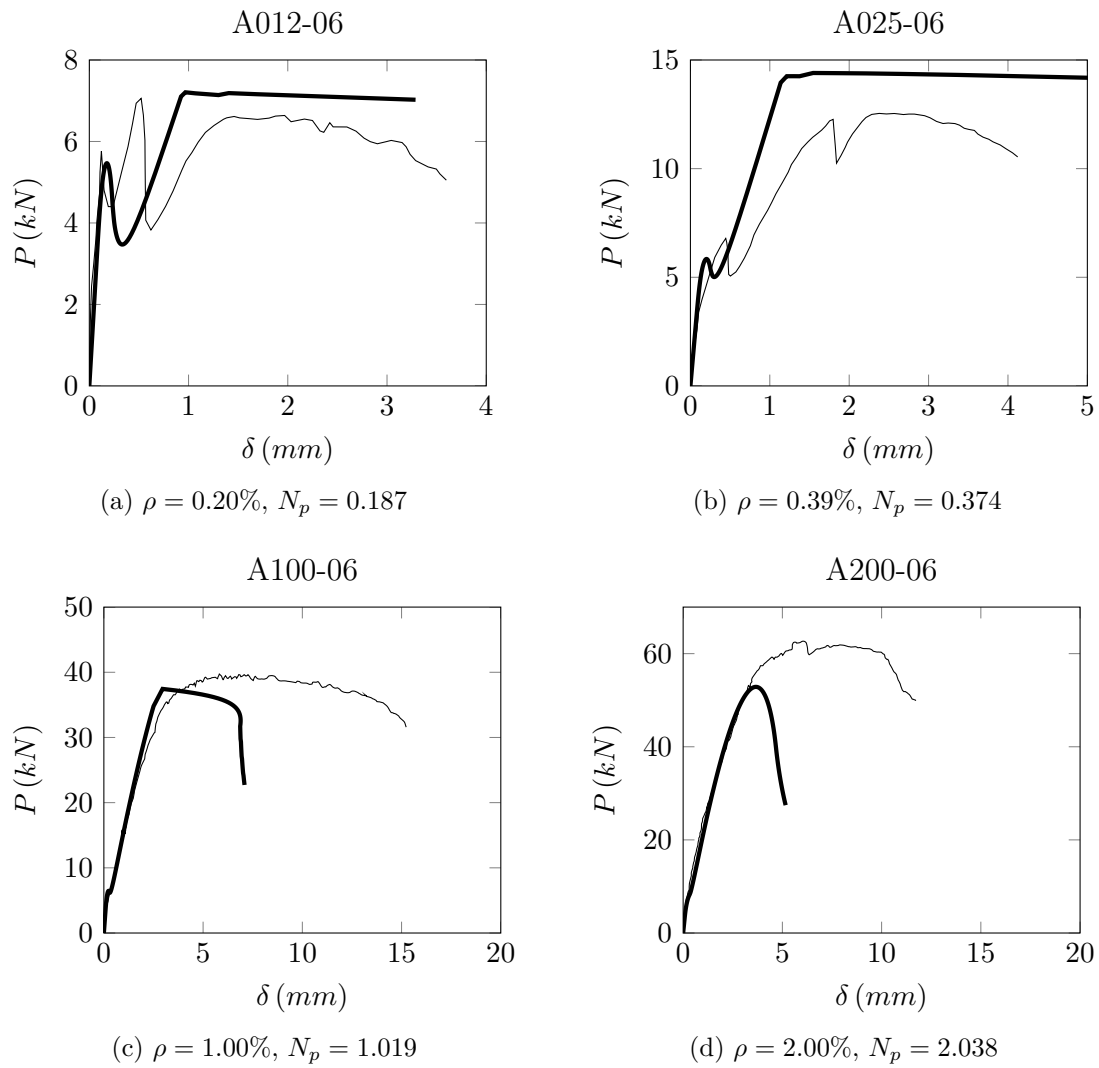


Figure 6.4: Numerical (thick curve) vs. experimental curves for specimens from A012-06 to A200-06

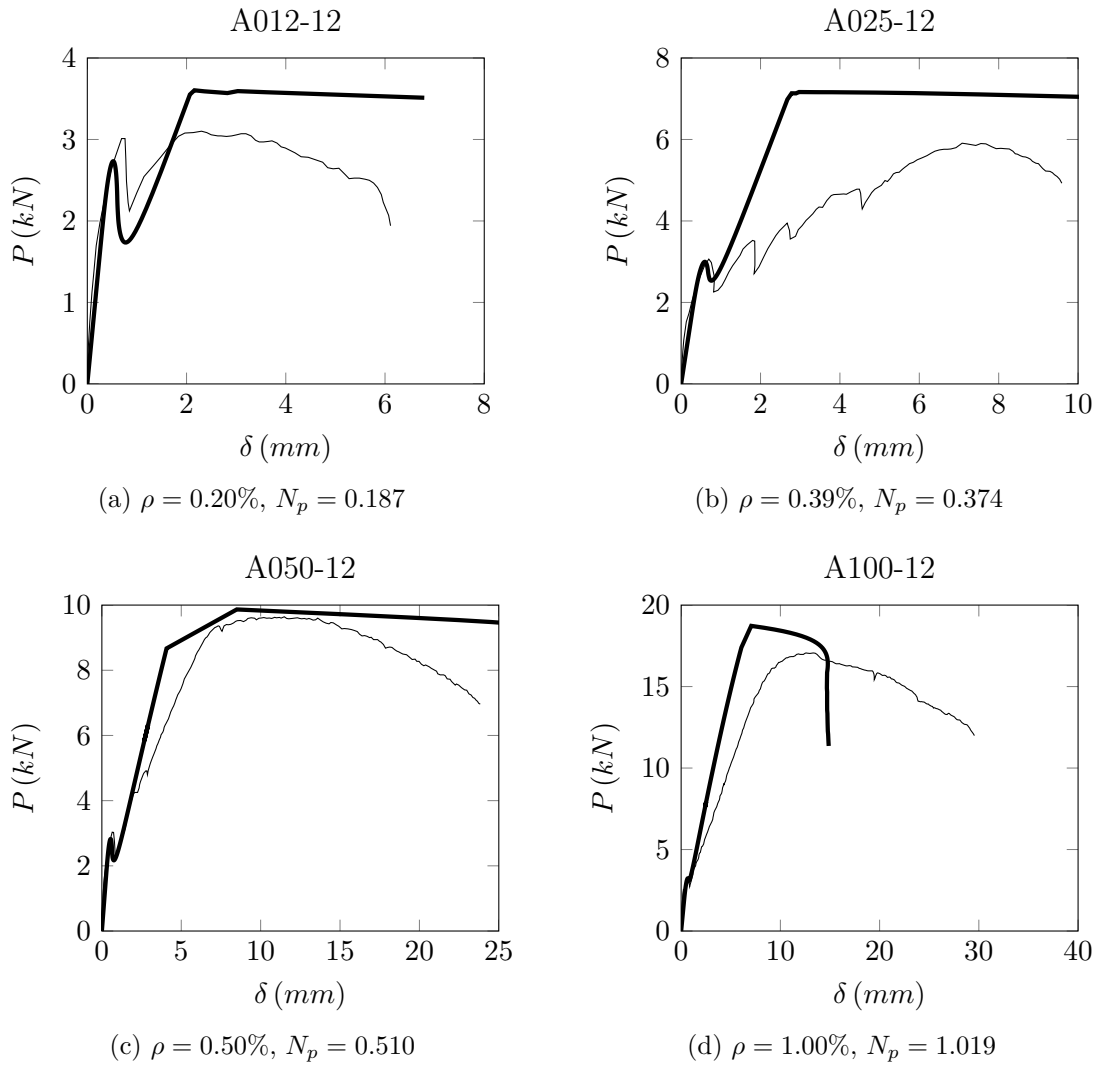


Figure 6.5: Numerical (thick curve) vs. experimental curves for specimens from A012-12 to A100-12

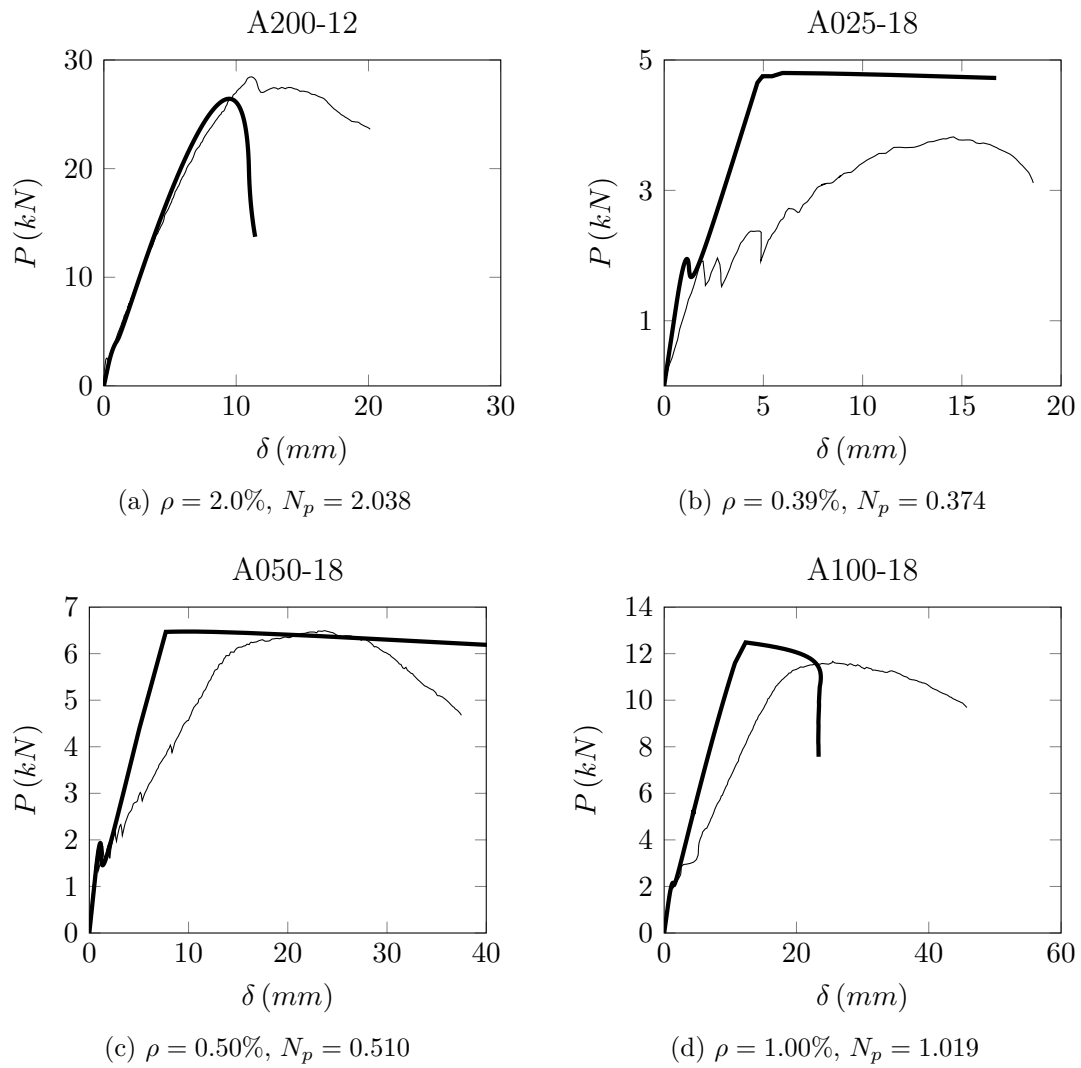


Figure 6.6: Numerical (thick curve) vs. experimental curves for specimens from A200-12 to A100-18

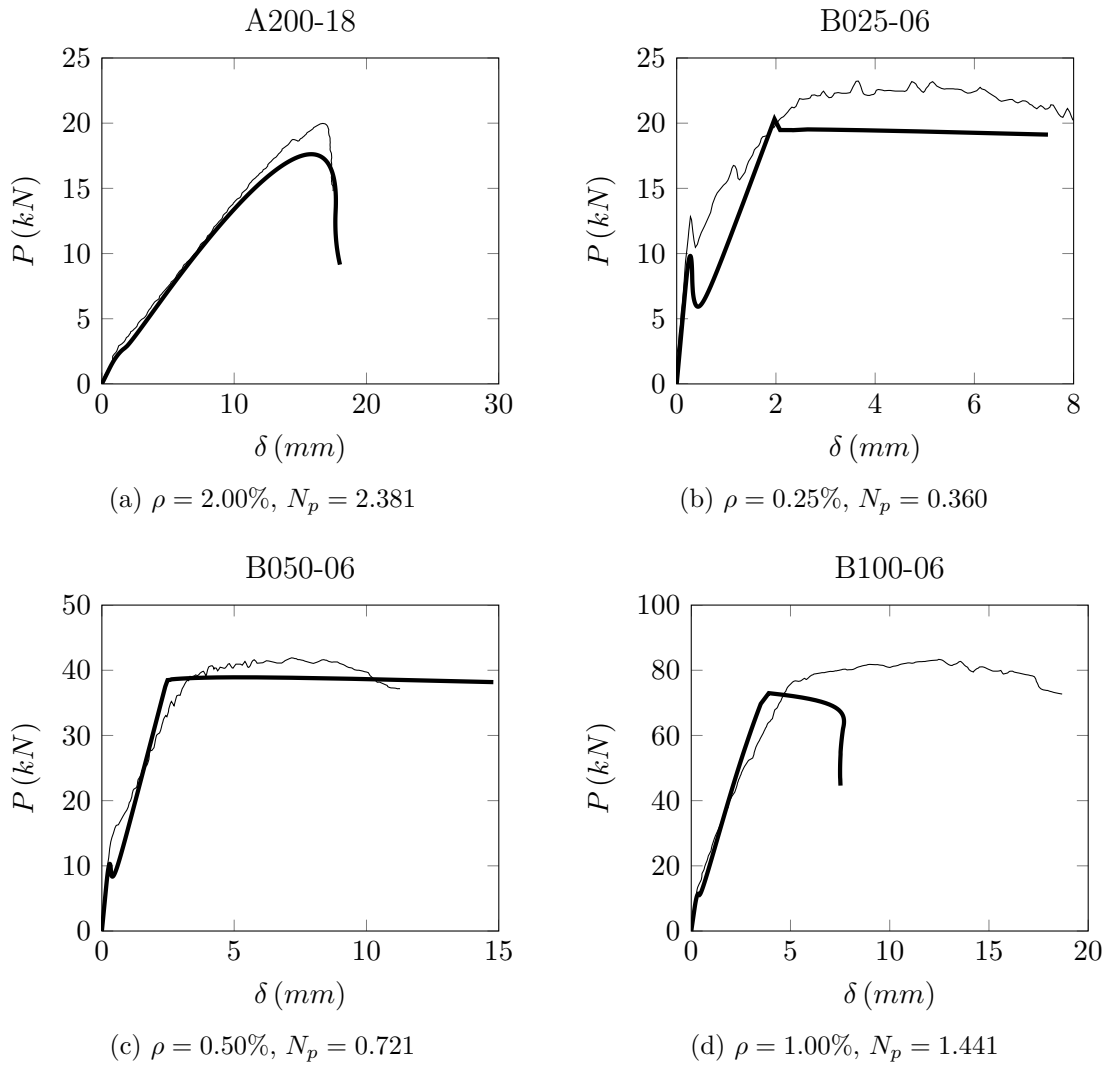


Figure 6.7: Numerical (thick curve) vs. experimental curves for specimens from A200-18 to B100-06

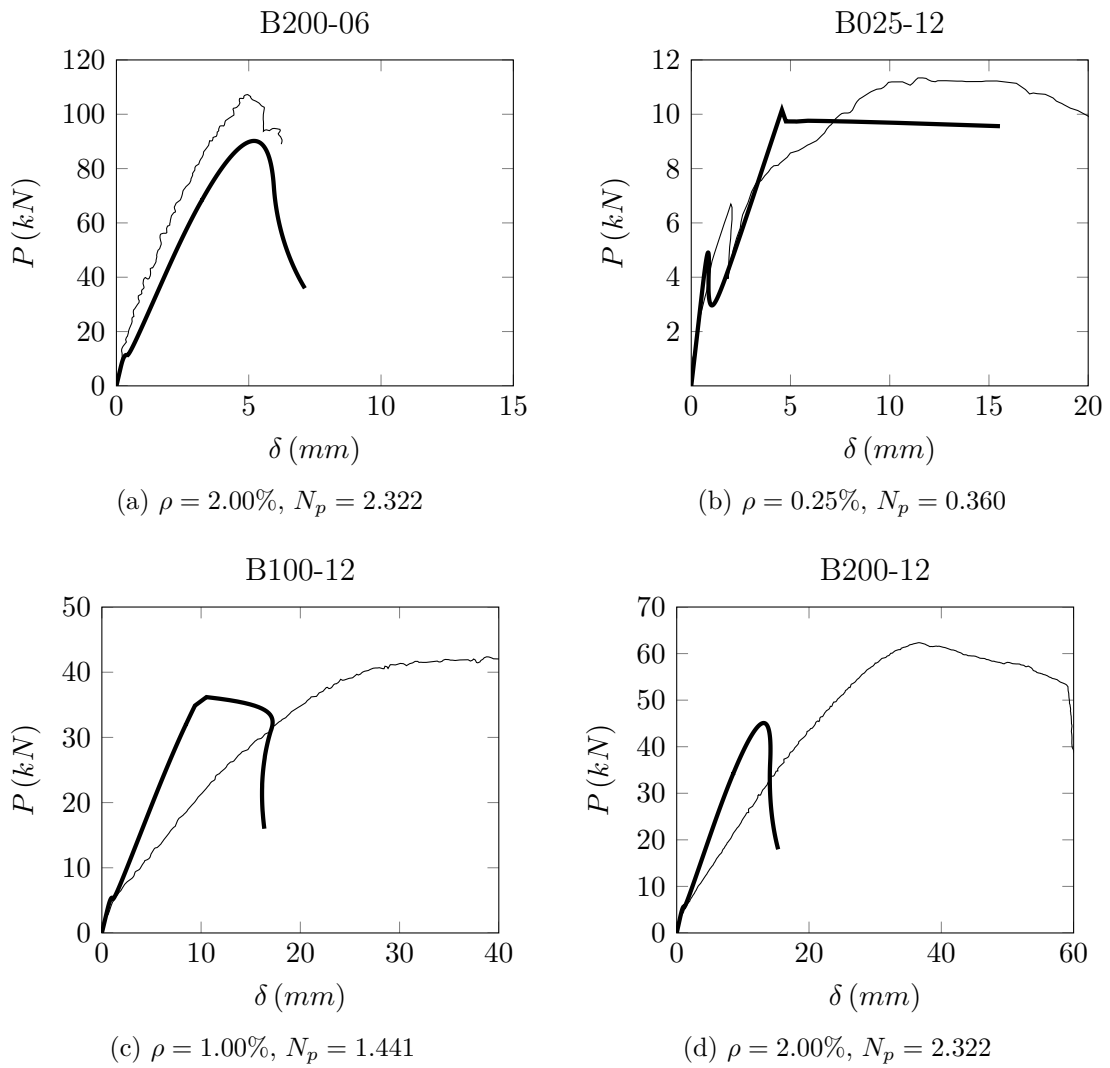


Figure 6.8: Numerical (thick curve) vs. experimental curves for specimens from B200-06 to B200-12

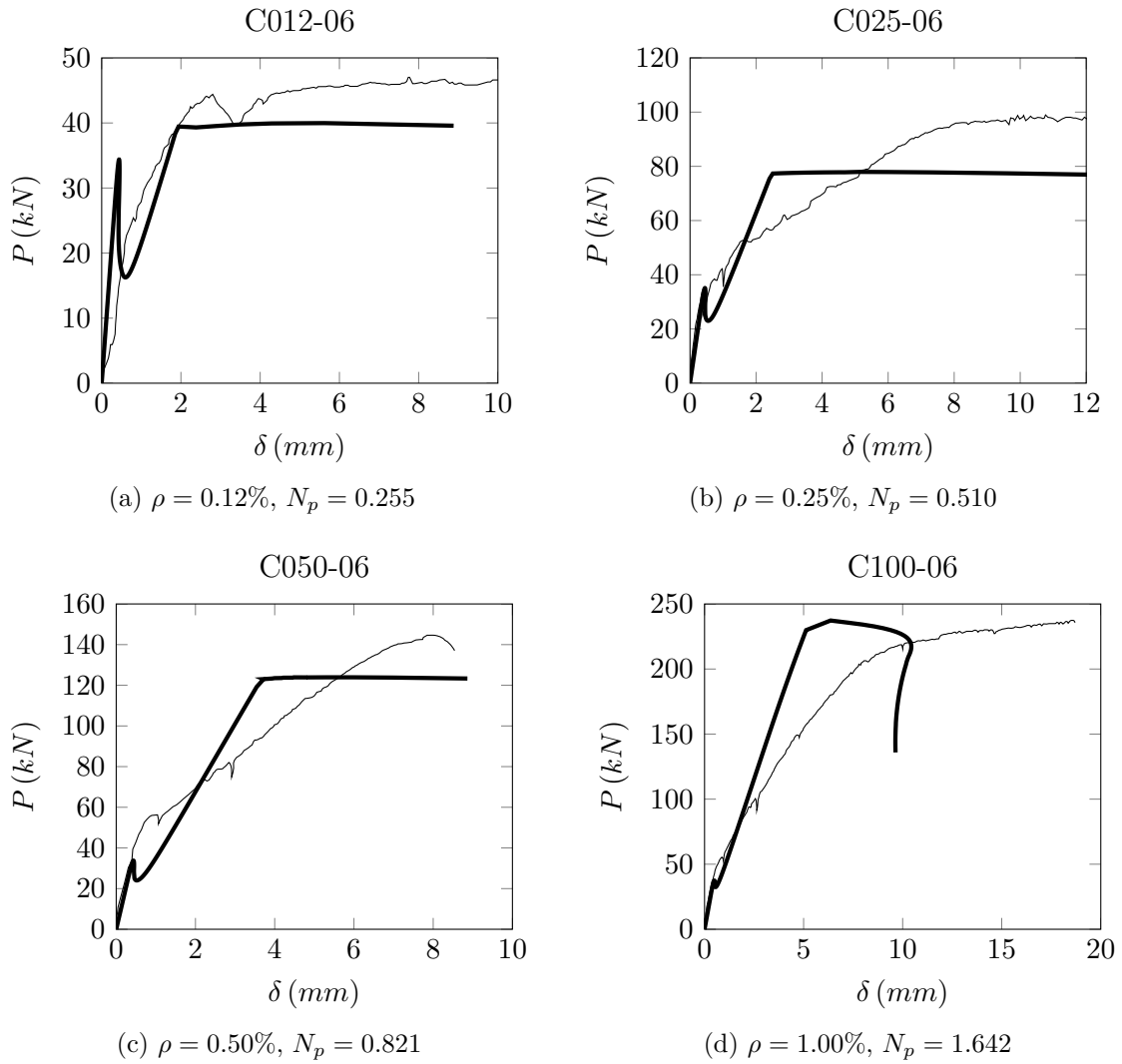


Figure 6.9: Numerical (thick curve) vs. experimental curves for specimens from C012-06 to C100-06

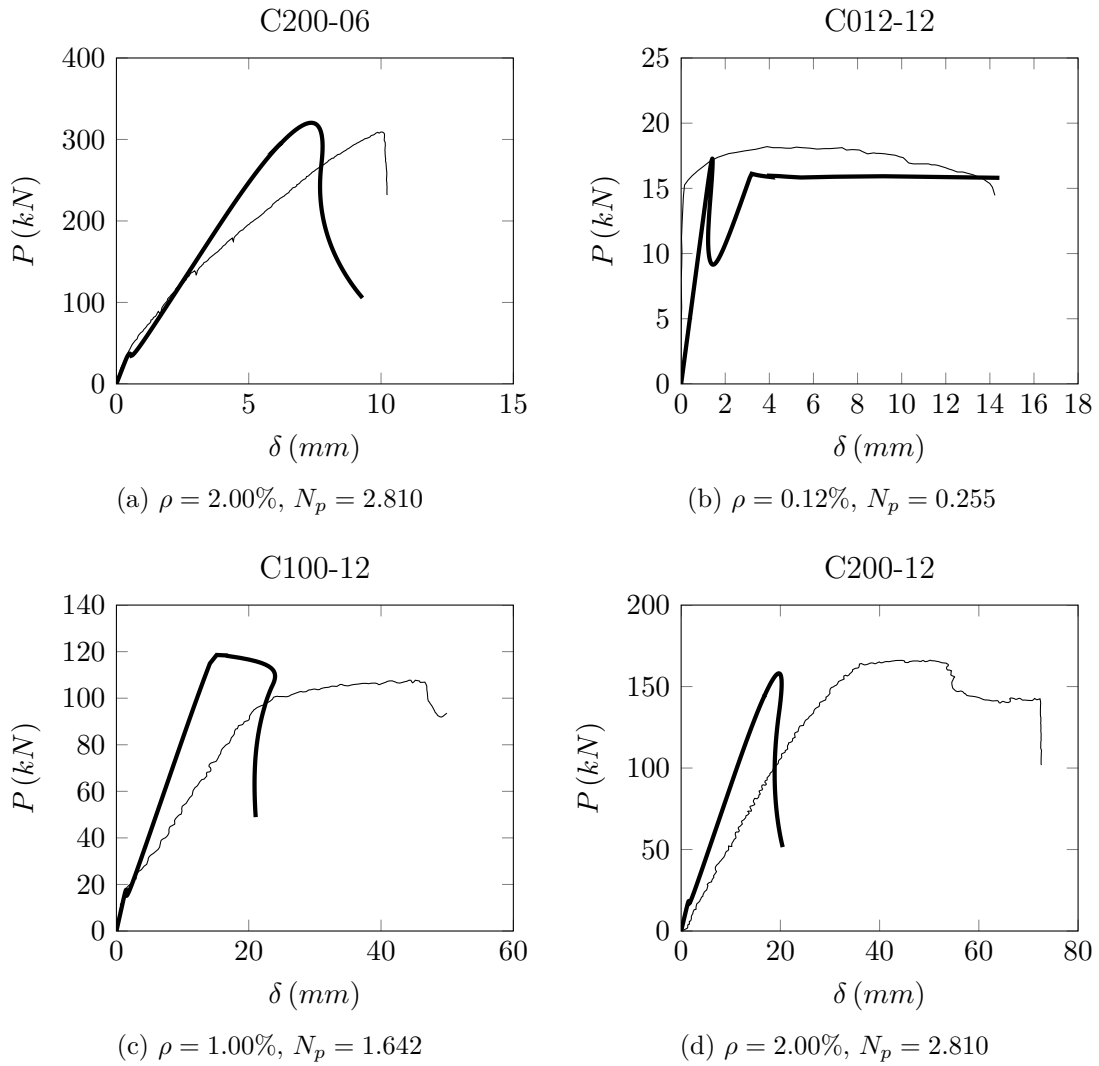


Figure 6.10: Numerical (thick curve) vs. experimental curves for specimens from C200-06 to C200-12

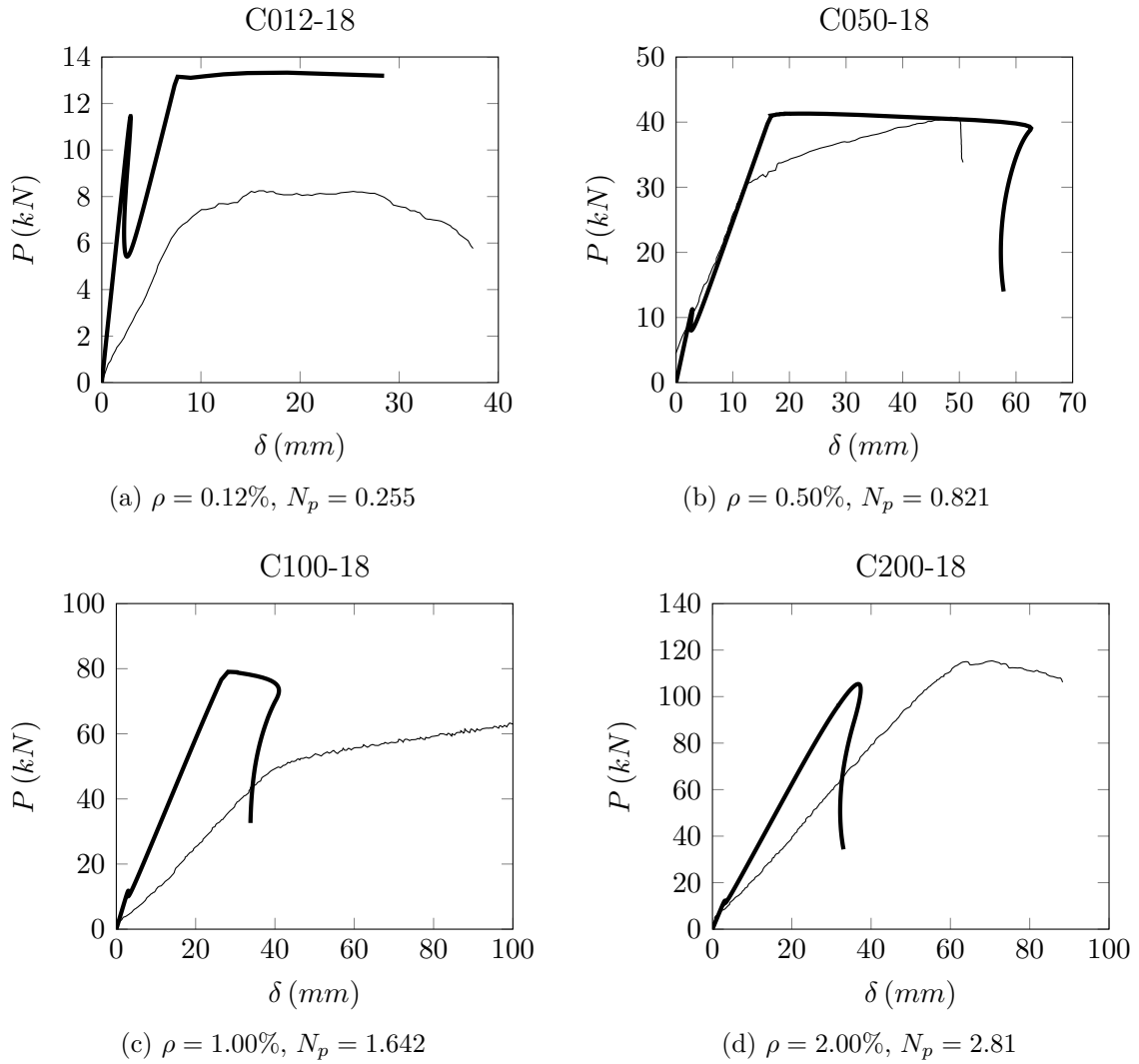


Figure 6.11: Numerical (thick curve) vs. experimental curves for specimens from C012-18 to C200-18

Chapter 7

Minimum reinforcement

In this chapter, the new numerical algorithm based on the cohesive and overlapping models will be used to estimate the minimum reinforcement percentage. Hence, national and international Code provisions are reported and compared, their shortcomings are underlined and a new formulation is proposed based on studies on this topic, carried by Carpinteri et al. [62, 63], by means of dimensional analysis.

7.1 Codes provisions

The tensile strength of concrete is usually neglected in the limit analysis of reinforced concrete beams. In the case of members having a large cross sectional area with a low steel percentage, this assumption may not lead to a safe design: if a section of the beam cracks, the force that prior to cracking was born partially by reinforcement and partially by concrete is forced to exploit steel and if the resistance of the cracked section is lower than the resistance of the uncracked section, the brittle failure of the structural member occurs [64]. Hence, national and international Codes impose to respect a minimum steel percentage which usually depends on concrete grade and steel yielding point. Thus, it is possible to find the minimum steel percentage as:

$$\gamma M_u = M_{cr} \tag{7.1}$$

where γ is a resistance factor, M_u and M_{cr} are the ultimate bending moment and the cracking bending moment, respectively. Hence, using the classical beam

theory, it is possible to rewrite the eqn. 7.1 as:

$$\gamma A_s f_{yk} d = f_{ctm} \frac{tb^2}{6} \quad (7.2)$$

Assuming a ratio $b/d = 1.2$ and $\gamma = 0.9$, it is possible to obtain the minimum reinforcement provision according to Model Code 2010 [58] and Eurocode 2 [65]:

$$A_{s,mim} = 0.26 \frac{f_{ctm}}{f_{yk}} bt \geq 0.0013bt \quad (7.3)$$

Other Codes provisions are based on the same assumptions [66–70] and some relations are reported:

$$BS8110 - 1 : 1997 \quad A_{s,mim} = 0.13bt \quad (7.4a)$$

$$ACI318 - 11 \quad A_{s,mim} = 0.25 \frac{\sqrt{f_{ck}}}{f_{yk}} bt \geq 1.4 \frac{bt}{f_{yk}} \quad (7.4b)$$

$$AS3600 - 2001 \quad A_{s,mim} = 0.22 \left(\frac{b}{d}\right)^2 \frac{f_{ctm}}{f_{yk}} bt \quad (7.4c)$$

$$IS456 : 2000 \quad A_{s,mim} = 0.85 f_{yk} bt \quad (7.4d)$$

$$NS3473 \quad A_{s,mim} = 0.35 k_w A_c f_{ctk,005} f_{yk} \quad (7.4e)$$

with $k_w = (1.5 - b) \geq 1$ in 7.4e.

In fig. 7.2 a comparison between national and international Codes provisions is provided. It may be seen that only the NS3473 E takes into account the size effect and indeed, it imposes a decreasing steel amount up to $b = 0.6 m$ and a constant value equal to $\rho = 0.23\%$ beyond this limit. The national Code that requires the highest minimum steel percentage is the ACI318-11 while the IS456:2000, the AS 3600-2011, the MC10 impose an almost equal quantity.

7.2 Numerical models for minimum reinforcement

The bridged crack model, based on LEFM, has been significantly used in the estimation of the minimum reinforcement [60, 71, 72]. The model considers a cracked RC element with a reinforcement layer and, by means of the superposition principle, defines the critic value of the stress intensity factor K_{IC} for which crack propagates.

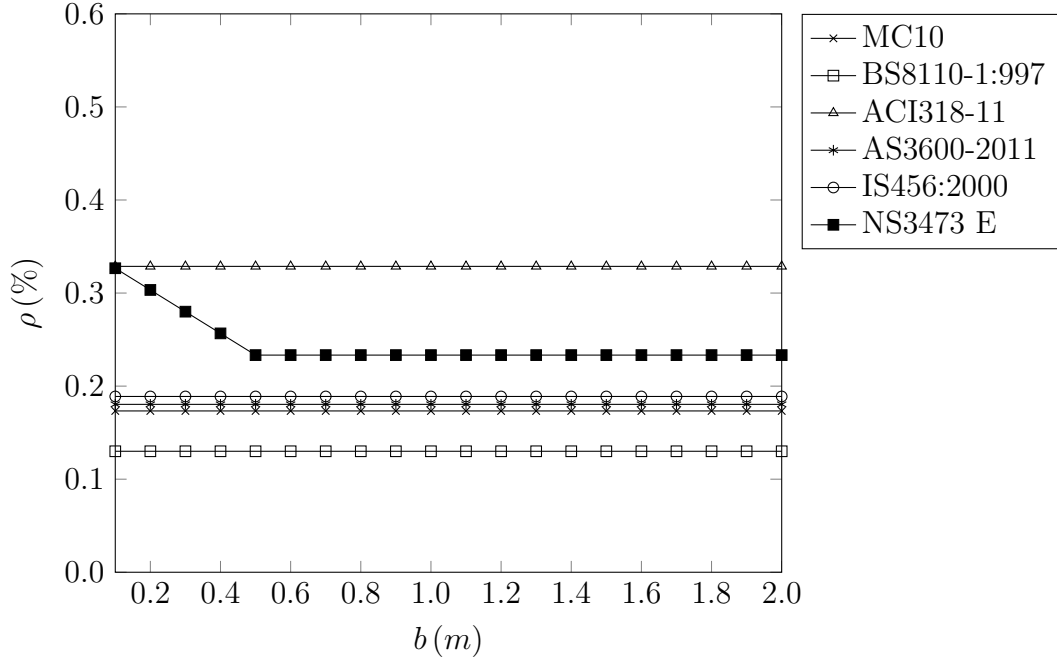


Figure 7.1: Comparison between minimum reinforcement Codes provisions

Furthermore, the value of the force exerted by steel is calculated assuming a kinematical condition on crack faces: the crack opening is assumed null up to steel layer yielding.

The global behaviour of the mechanical system is completely described by the *reinforcement brittle number* N_P :

$$N_P = \rho \frac{\sigma_y b^{0.5}}{K_{IC}} \quad (7.5)$$

The value of N_P for which the minimum reinforcement condition is reached is called N_{PC} and, it is a function of the concrete grade:

$$N_{PC} = 0.1 + 0.0023 f_{cm} \quad (7.6)$$

Equalling the eqn. 7.5 and eqn. 7.6, it is possible to calculate the minimum reinforcement according to the bridged crack model:

$$A_{s,mim} = \frac{K_{IC}}{f_{yk}} (1 + 0.0023 f_{cm}) t b^{0.5} \quad (7.7)$$

Other formulations that it is possible to find in literature [57, 73–77] based on several models are reported:

$$\text{Hawkins and Hjortset} \quad \rho_{s,mim} = 0.183 \left(1 + \frac{1}{0.85 + 2.3b/l_{ch}} \right) \frac{f_{ctm}b}{f_{yk}(b-c)} \quad (7.8a)$$

$$\text{Ruiz et al.} \quad \rho_{s,mim} = \frac{0.175}{1-\gamma} \cdot \frac{1 + (0.85 + 2.3\beta_1)^{-1}}{f_{yk}^* - \eta_1\varphi} \quad (7.8b)$$

$$\text{Gerstle et al.} \quad \rho_{s,mim} = \frac{E_c}{E_s} \left(\sqrt{0.0081 + 0.0148 \frac{f_{ctm}b}{E_c w_{cr}^t}} - 0.0900 \right)^{0.5} \quad (7.8c)$$

$$\text{Baluch et al.} \quad \rho_{s,mim} = \frac{1.9134K_{IC}}{f_{yk}^{0.9922} (1.7 - 2.6c/b)} \quad (7.8d)$$

$$\text{Appa Rao et al.} \quad \rho_{s,mim} = \left(-0.01 + \frac{40.10}{d} \right) \frac{f_{ck}^{1.14}}{f_{yk}^{0.57}} \quad (7.8e)$$

$$\text{Shehata et al.} \quad \rho_{s,mim} = 0.5 \frac{f_{ck}^{0.67} (1 + 1.5b)}{f_{yk} b^{0.7}} \quad (7.8f)$$

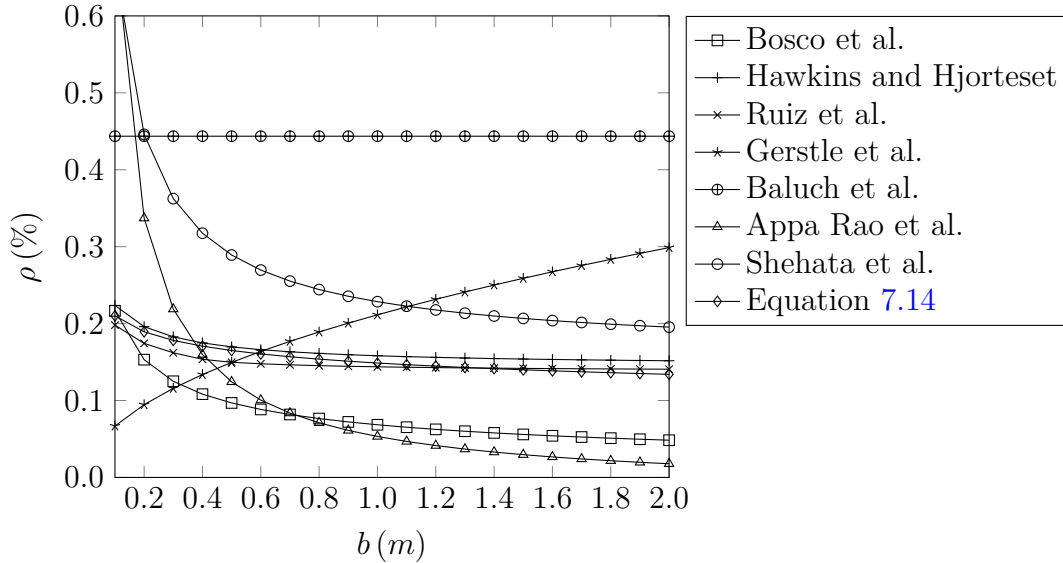


Figure 7.2: Minimum reinforcement vs. effective beam depth according to various models

being: $l_{ch} = E_c G_f / f_{ctm}^2$, $\beta_1 = b / (\alpha l_{ch})$, $\alpha = (65 + 15d_{max}/8) / 170$ with d_{max} maximum aggregate size, $f_y^* = f_{yk} / f_{ctm}$, $\eta_1 = 15$, $\varphi = (\beta_1^{0.25} - 3.6c/b \cdot \beta_1) \geq 0$.

In fig. 7.2 the eqn. 7.14 refers to a new formulation that will be presented in the next section. It may be seen that apart from Gerstle et al., all the formulations

furnish a minimum reinforcement that is inversely proportional to the beam depth. More precisely, it is possible to work out as the relations of Hawkins and Hjortset, Ruiz et al. and eqn. 7.11 provide a minimum reinforcement that is quite similar since they are based on the same model, i.e. the cohesive model. Shehata et al. and Appa Rao et al. formulations presents a minimum reinforcement that is highly dependent on the beam depth, while Bosco et al. provides a reinforcement percentage below 0.1% for large size beams.

7.3 Dimensional analysis approach

It is possible to use the Buckingham's theorem [78] to point out the quantities that contribute in the definition of the minimum reinforcement. Hence, it is possible to write:

$$M = g(f_{ctm}, G_F, E_c, f_{yk}, A_s, b; \vartheta) \quad (7.9)$$

where f_{ck} and G_C are neglected since in lightly reinforced beam the crushing of concrete does not take place. Hence, assuming K_{IC} and b as fundamentals parameters and minimizing the problem space it is possible to obtain:

$$\frac{M}{b^{2.5}K_{IC}} = g_1\left(\frac{f_{ctm}b^{0.5}}{K_{IC}}, \frac{A_s f_{yk}b^{0.5}}{bt K_{IC}}, \vartheta \frac{E_c b^{0.5}}{K_{IC}}\right) \quad (7.10)$$

where it is possible to recognize the stress brittleness number s and the reinforced brittleness number N_P .

Thus, a numerical investigation may be carried out in order to identify the relationship between the two non-dimensional numbers.

The concrete grades that have been simulated are reported in tab. 7.1: the modulus of elasticity E_c has been varied between 2.2 to 4.8 *GPa*, the tensile strength of concrete has been calculated as:

$$f_{ctm} = 0.3 f_{ck}^{2/3} \leq C50/60 \quad (7.11a)$$

$$f_{ctm} = 2.12 \cdot \log\left(1 + \frac{f_{cm}}{10}\right) > C50/60 \quad (7.11b)$$

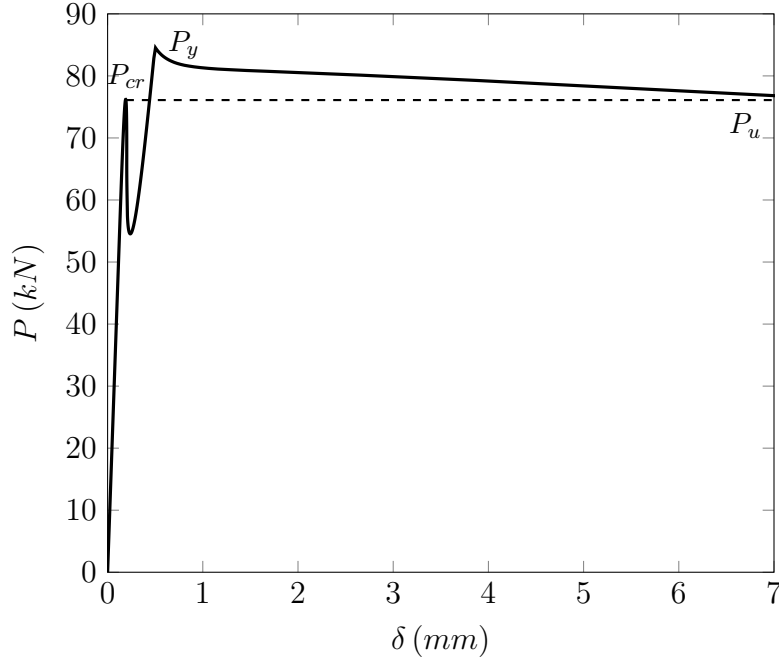


Figure 7.3: Minimum reinforcement condition for a beam: $b = t = 400 \text{ mm}$, $\lambda = 4$, $f_{ctm} = 2.2 \text{ mm}$, $G_F = 0.062 \text{ N/mm}$, $E_c = 30 \text{ GPa}$, $\rho = 0.124\%$, $d/b = 0.9$

while the energy release rate G_F has been computed through the relation provided by Model Code 90:

$$G_F = G_{F0} \cdot \left(\frac{f_{cm}}{f_{cm0}} \right)^{0.7} \quad (7.12)$$

where G_{F0} is the base value of the fracture energy that depends on the maximum size of the aggregate (which has been fixed to 16 mm) and $f_{cm0} = 10 \text{ MPa}$. The numerical simulations have been carried fixing the ratio $d/b = 0.9$, a square cross sectional area and a slenderness ratio equal to 4.

The numerical studies have been carried varying the steel percentage until the equalling between the cracking load P_{cr} and the ultimate load P_u , as reported in fig. 7.3, has been found.

The resulted $A_s/(tb)$ ratios, the values s and N_{PC} are reported in tab. 6.1.

It is possible to realize a plot of N_{PC} vs. s in order to find a trend for minimum reinforcement percentage as suggested by eqn. 7.10. Thus, the numerical results are

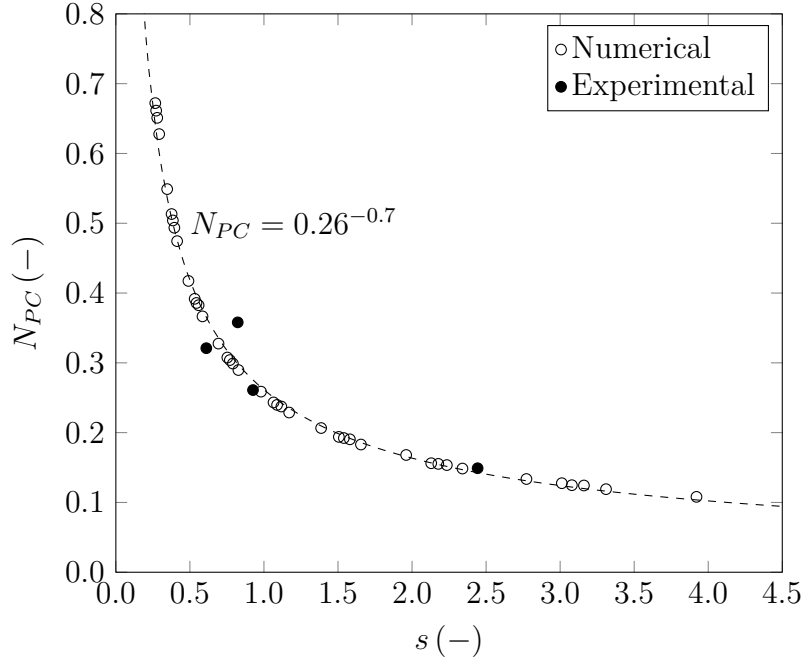


Figure 7.4: Best-fit relationship of numerical results in the plane s - N_{PC}

reported in fig. 7.4 and it may be seen that the following hyperbolic curve represents the best-fit of the numerical simulations¹:

$$N_{PC} = 0.26s^{-0.7} \quad (7.13)$$

Hence, substituting the definition of N_{PC} and s in eqn. 7.13, it is possible to obtain:

$$A_{s,min} = 0.26 \frac{f_{ctm}^{0.7} K_{IC}^{0.3}}{f_{yk}} t b^{0.85} \quad (7.14)$$

¹In fig. 7.4, black dots refer to minimum reinforcement percentages experimentally observed [73, 79].

f_{ck} (MPa)	f_{ctm} (MPa)	G_F (N/mm)	E_c (GPa)	b (mm)	A_s/bt (mm)	N_{PC} (-)	s (-)
20	2.2	0.062	30	25	0.207	0.108	3.921
				50	0.181	0.134	2.772
				100	0.161	0.168	1.960
				200	0.140	0.207	1.386
				400	0.124	0.259	0.980
				800	0.111	0.328	0.693
				1600	0.100	0.417	0.490
				3200	0.093	0.549	0.347
35	3.2	0.083	34	25	0.281	0.119	3.921
				50	0.248	0.149	2.772
				100	0.216	0.183	1.960
				200	0.191	0.229	1.386
				400	0.171	0.290	0.980
				800	0.153	0.367	0.693
				1600	0.140	0.474	0.490
				3200	0.131	0.628	0.347
50	4.1	0.103	37	25	0.350	0.128	3.921
				50	0.300	0.156	2.772
				100	0.266	0.194	1.960
				200	0.242	0.243	1.386
				400	0.220	0.308	0.980
				800	0.200	0.392	0.693
				1600	0.183	0.513	0.490
				3200	0.173	0.672	0.347
65	4.5	0.120	40	25	0.384	0.125	3.921
				50	0.338	0.155	2.772
				100	0.296	0.192	1.960
				200	0.261	0.240	1.386
				400	0.234	0.304	0.980
				800	0.210	0.386	0.693
				1600	0.194	0.504	0.490
				3200	0.180	0.661	0.347
80	4.8	0.137	42	25	0.419	0.124	3.921
				50	0.366	0.154	2.772
				100	0.321	0.190	1.960
				200	0.283	0.237	1.386
				400	0.252	0.299	0.980
				800	0.228	0.383	0.693
				1600	0.208	0.494	0.490
				3200	0.194	0.651	0.347

Table 7.1: Mechanical parameters for the beams considered in the numerical simulations

Chapter 8

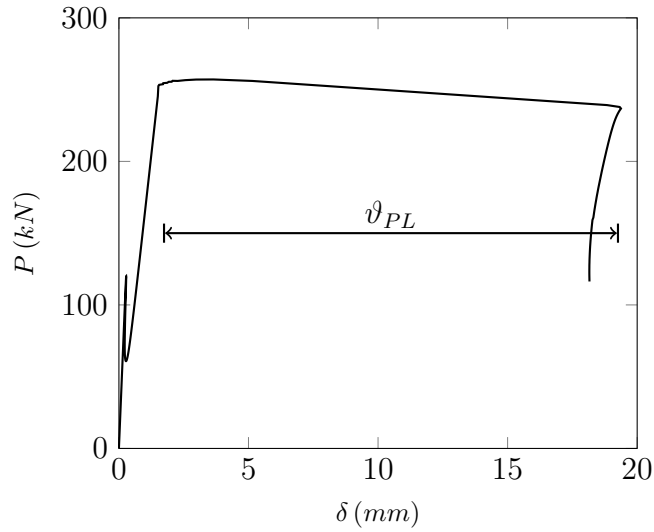
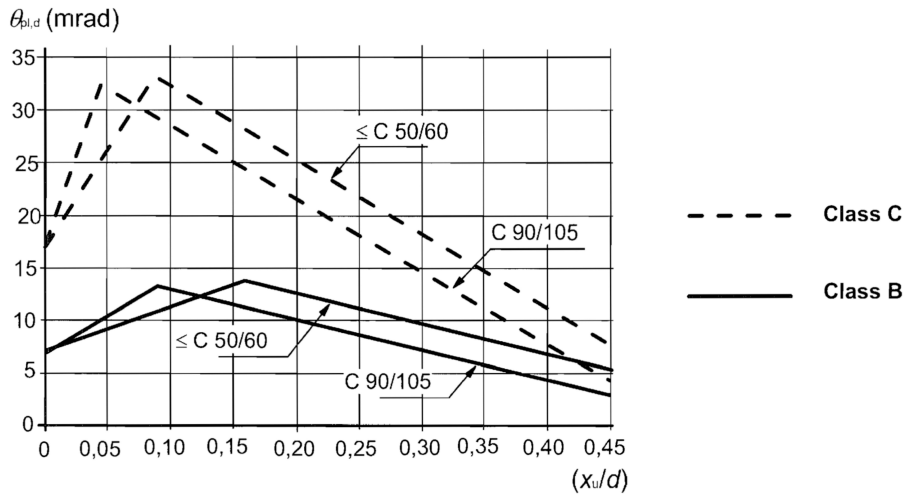
Rotational capacity of beams

The ductility of a structure may be evaluated as the *rotational capacity* ϑ_{PL} of the plastic hinges, calculated as the rotation difference between the ϑ beyond which a drop in the load carry capacity is registered, and the θ corresponding to steel yielding as depicted in fig. 8.1. Between the years 1960 and 1965, a C.E.B. Commission supported a long series of tests on reinforced concrete beams in order to highlight the fundamental parameters that influence the rotational capacity of concrete members. The results of these tests have been numerically studied and Siviero [80] has proposed the following formulation:

$$\vartheta_{PL} = 0.004 \frac{x}{d} \quad (8.1)$$

being x/d the relative neutral axis depth at the ultimate limit state. In the same years, other authors proposed to calculate ϑ_{PL} referring to the definition of length of plastic hinge and first attempts to take into account also the shear contribution were proposed.

Nevertheless, the most important problem of all the numerical models proposed in that years is the overestimation of ϑ_{PL} since they assumed always the concrete failure in compression; only the research group headed by Prof. Eligehausen [81] formulated an analytical model that was able to take into account both steel and concrete failure: for low values of x/d the rupture of steel occurs whereas for large

Figure 8.1: v_{PL} definitionFigure 8.2: v_{PL} - x/d relation according to Eurocode 2

x/d values, the concrete crushing becomes more and more important. This concept has been accepted by Eurocode 2 [65] which proposes the diagram depicted in fig. 8.2 to calculate the plastic resources of a structure.

On the other hand, the size effect is completely neglected. In fig. 8.3 are plotted rotational capacity results obtained by the application of the new cohesive/ overlapping algorithm for several beam depths, steel percentage and the Eurocode 2 prediction. In this figure, it is possible to observe that the numerical results provide

a lower ϑ_{PL} values suggesting that rotations assumed by the Code are not always conservative. This conclusion is confirmed by the fig. 8.4 in which are reported rotations provided by the numerical algorithm and Eurocode 2 for the experimental test of beams reported in tab. 6.1. It is worth noticing that except for beams A050-12, B025-12, B050-06, the numerical procedure provide values that are nearer the experimental results than the Code predictions.

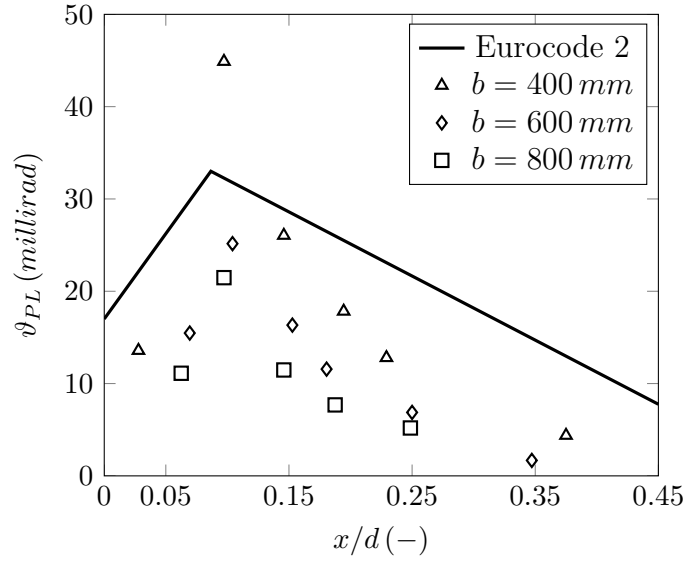


Figure 8.3: Rotation for different beam heights compared with Eurocode 2 predictions

8.1 Dimensional analysis approach

In order to outline the fundamental parameters influencing ϑ_{PL} , it is possible to adopt the dimensional analysis approach [82, 83]. Hence, it is possible to write the following relationship:

$$M = g_1 \left(f_{ctm}, G_F, f_c, G_C, E_c, f_{yk}, \rho, b; \frac{t}{b}, \frac{l}{b}, \vartheta \right) \quad (8.2)$$

Since we are interested in the study of over-reinforced beams in bending (it has been demonstrated that low reinforced beams have wide plastic plateau), it is possible to neglect in the eqn. 8.2 the terms f_{ctm} and G_F . Thus, assuming b and

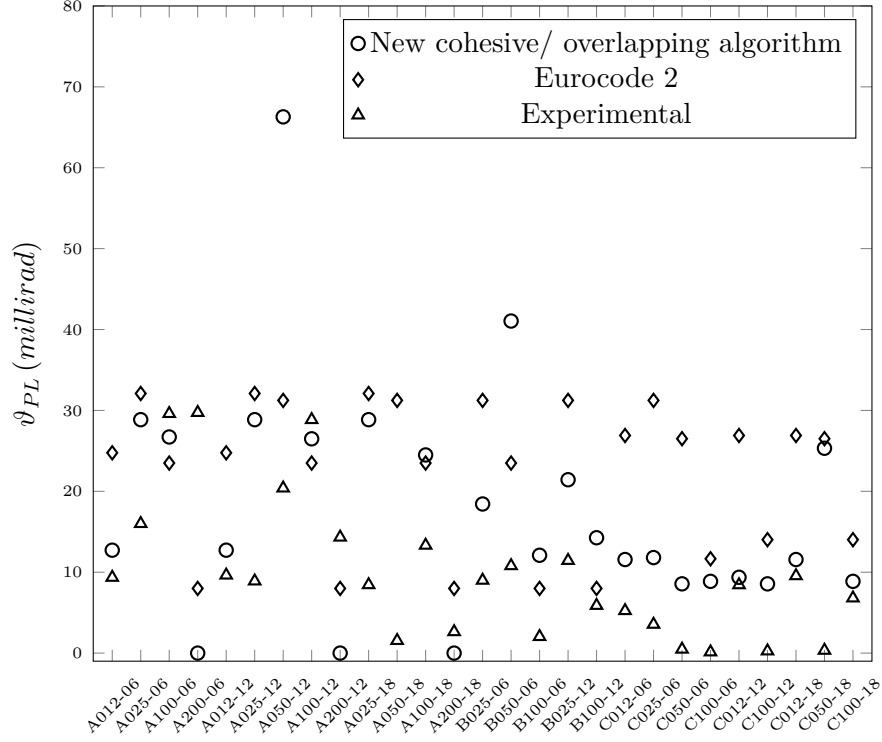


Figure 8.4: Rotational capacity comparison

$\sqrt{G_C E_C}$ as fundamental variables, it is possible to write:

$$\frac{M}{\sqrt{G_C E_c} b^{5/2}} = g_1 \left(\frac{f_c b^{1/2}}{\sqrt{G_C E_c}}, \rho \frac{f_{yk} b^{1/2}}{\sqrt{G_C E_c}}, \vartheta \frac{b^{1/2} E_C}{\sqrt{G_C E_c}} \right) \quad (8.3)$$

where it is possible to recognize similar quantities defined in the eqn. 7.10 for the study of the minimum reinforcement ratio.

The eqn. 8.3 has been used to define through numerical simulations with the original cohesive/overlapping algorithm (for more details see the articles cited at the beginning of the present section) a relation that is able to define the maximum steel percentage in a structural member. The ρ_{max} percentage depends on the beam depth and is defined as the maximum steel beyond which no plastic resources are exploited due concrete failure in compression.

Chapter 9

The effect of a pre-stressing force

The numerical algorithm presented in chapter 5 may be modified conveniently in order to take into account the presence of a pre-stressing force. More precisely, the eqn. 5.7 may be modified as:

$$\{w\} = [K_F]\{F\} + \{K_M\}M + \{F_0\} \quad (9.1)$$

where $\{F_0\}$ represents the nodal forces generated by F_P .

The $\{F_0\}$ vector is calculated by means of the Navier formula. More precisely, the routine *ReinforcementData.m* is able to calculate the σ generated by the pre-stressing force and integrate them by means of the midpoint rule. Due to the inability of the current version of the algorithm to take into account the full-span behavior of the members, pre-stressing losses are neglected and the pre-stressing force is assumed to enter completely in the beam. Furthermore, the increase of force in the cable due to crack opening is assumed as a concentrated force directly applied on crack faces.

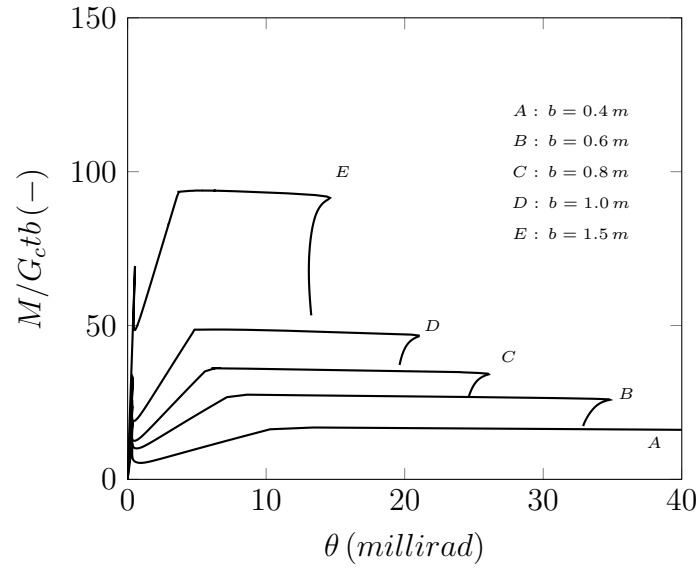
In the following section several rotation vs. non-dimensional load diagrams will be presented for pre-stressing members varying both pre-stressing steel percentage and beam depth.

9.1 Numerical investigation

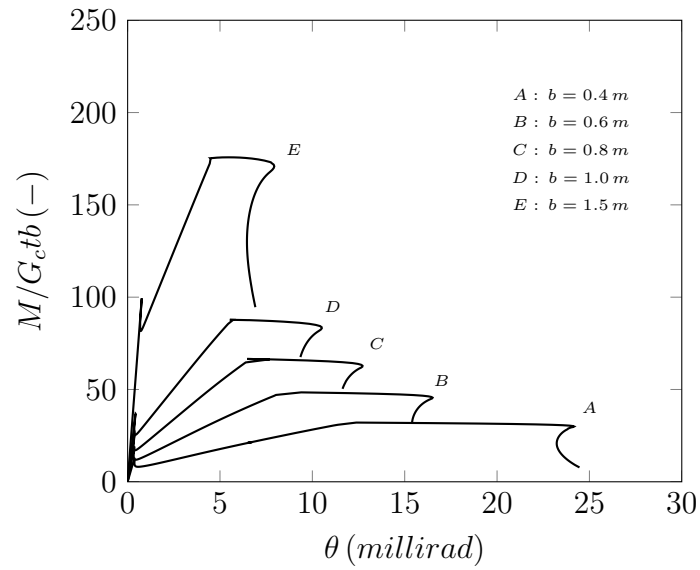
From fig. 9.1 to fig. 9.5, non-dimensional load vs. rotation diagrams for different pre-stressing steel ratio and beam heights are plotted. The steel constitutive law has been assumed elastic-perfectly plastic with $f_{01} = 1640 \text{ MPa}$, the ratio d/b has been set equal to 0.9 and the pre-stressing force F_P has been assumed $F_P = 1/3 f_{01} A_{sp}$ for all the numerical simulations.

It may be seen that for low pre-stressing steel percentages, the behaviour is quite similar to reinforced beams: there is an ascending branch up to concrete cracking, a snap-back and then, a second ascending branch up to steel yielding. At the end of the plastic plateau, a snap-back in compression is revealed even for low structural scale.

In case of pre-stressed steel percentage bigger than 0.2% as depicted in fig. 9.2-9.5 there is no steel yielding and the failure that prevails is the crushing one and, the snap-back in compression appears to be more severe for bigger scale and larger pre-stressed beam reinforcement.

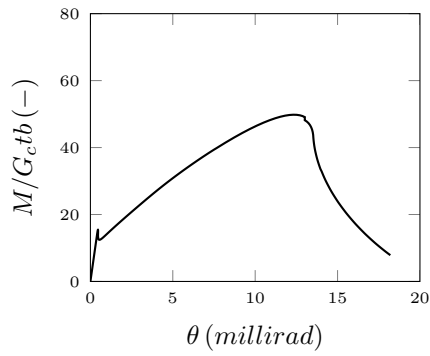


(a) Pre-stressing steel $\rho_p = 0.1\%$

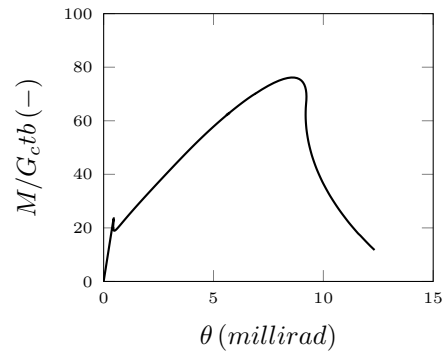


(b) Pre-stressing steel $\rho_p = 0.2\%$

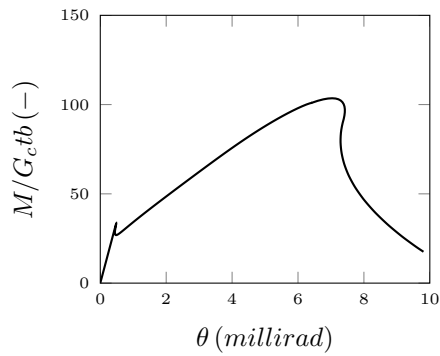
Figure 9.1: Non-dimensional load vs. rotation for pre-stressing steel having $\rho_p = 0.1\%$ (a) and $\rho_p = 0.2\%$ (b)



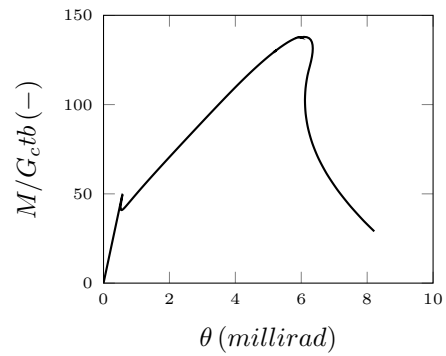
(a) Beam depth: $b = 400$ mm



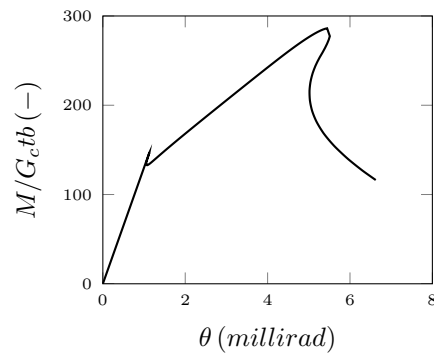
(b) Beam depth: $b = 600$ mm



(c) Beam depth: $b = 800$ mm

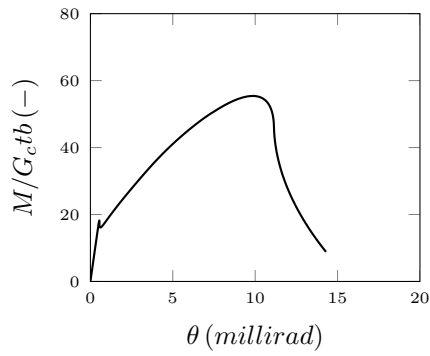


(d) Beam depth: $b = 1000$ mm

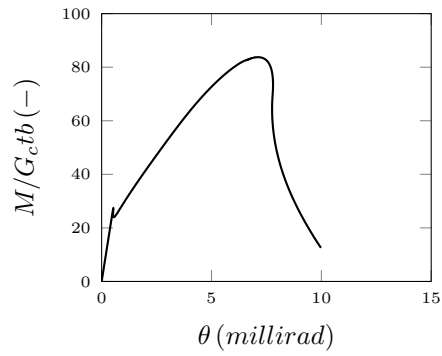


(e) Beam depth: $b = 1500$ mm

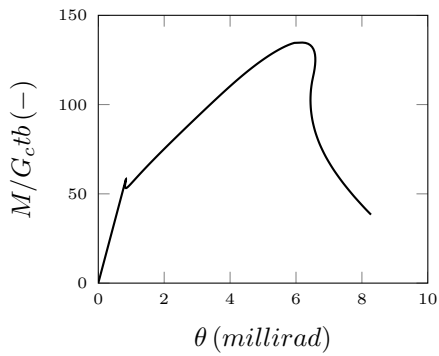
Figure 9.2: Non-dimensional load vs. rotation for pre-stressing beams having $\rho_p = 0.4\%$



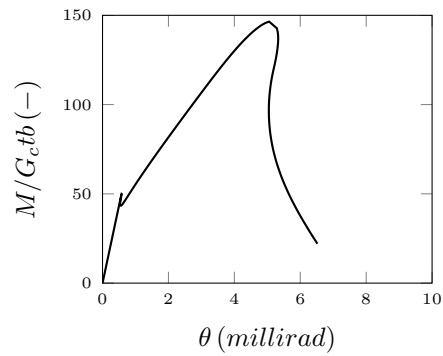
(a) Beam depth: $b = 400$ mm



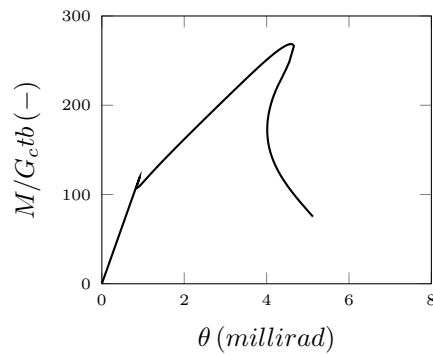
(b) Beam depth: $b = 600$ mm



(c) Beam depth: $b = 800$ mm

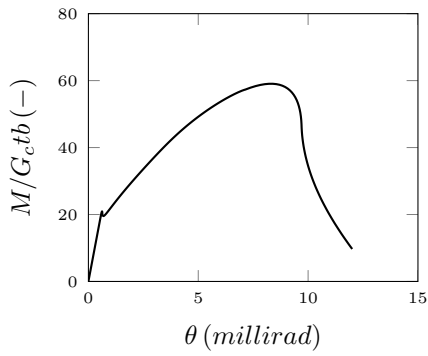


(d) Beam depth: $b = 1000$ mm

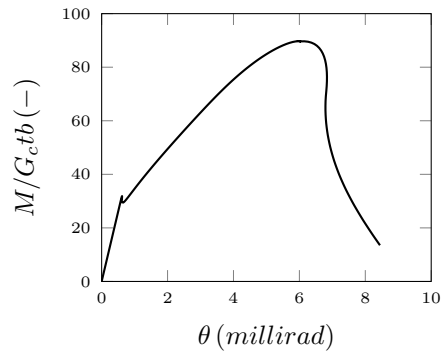


(e) Beam depth: $b = 1500$ mm

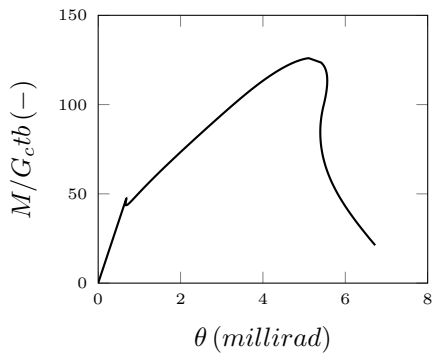
Figure 9.3: Non-dimensional load vs. rotation for pre-stressing beams having $\rho_p = 0.6\%$



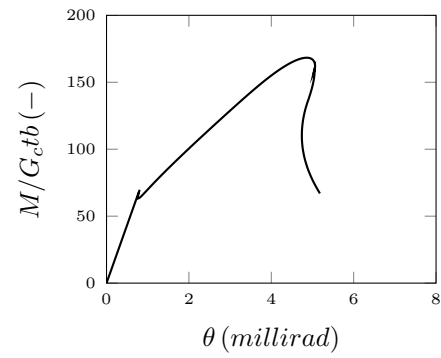
(a) Beam depth: $b = 400$ mm



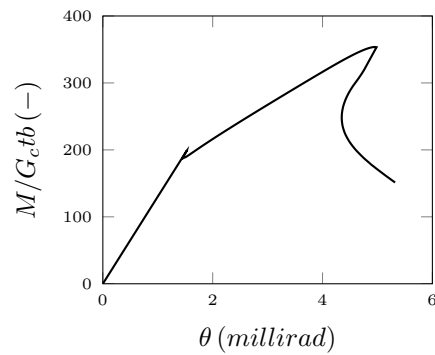
(b) Beam depth: $b = 600$ mm



(c) Beam depth: $b = 800$ mm

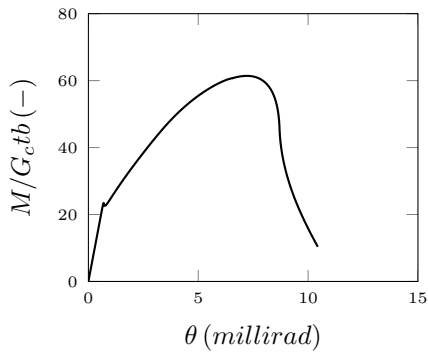


(d) Beam depth: $b = 1000$ mm

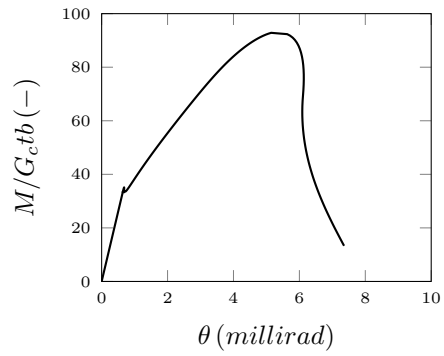


(e) Beam depth: $b = 1500$ mm

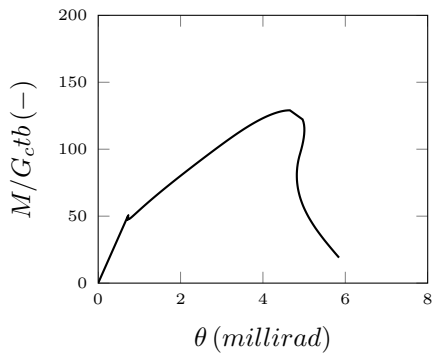
Figure 9.4: Non-dimensional load vs. rotation for pre-stressing beams having $\rho_p = 0.8\%$



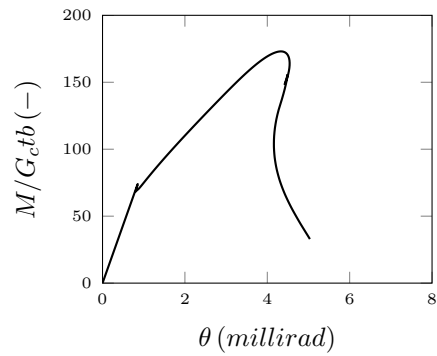
(a) Beam depth: $b = 400$ mm



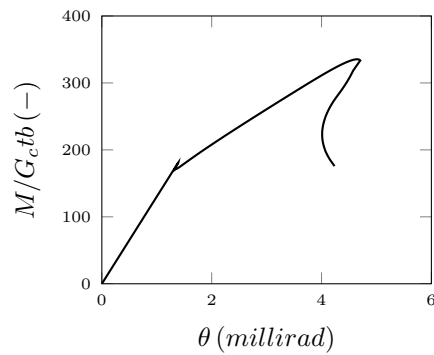
(b) Beam depth: $b = 600$ mm



(c) Beam depth: $b = 800$ mm



(d) Beam depth: $b = 1000$ mm



(e) Beam depth: $b = 1500$ mm

Figure 9.5: Non-dimensional load vs. rotation for pre-stressing beams having $\rho_p = 1.0\%$

Chapter 10

Future algorithm developments

The present work demonstrates the capability of the algorithm and, of the integration of the cohesive and overlapping crack models to be able to describe some non-linearities, such as crack opening, steel yielding and/or slippage and concrete crushing, that may occur during the loading process of a reinforced concrete beam. Furthermore, the numerical procedure herein proposed, is able to simulate the size-effect of concrete structural members that is often observed experimentally and neglected, in the design procedures and structures security assessment, for sake of simplicity. The current version of the program is able to simulate only Mode I crack propagation and, hence, the role of shear is completely neglected. In order to fill this gap, the numerical procedure may be improved and generalized considering the crack growing also in a Mode II condition allowing to simulate the beam in its full span. In this way a comprehensive representation of the transitions between structural collapse mechanisms will be given.

Indeed, as showed in fig. 10.1, the crack propagation (flexural failure), the damage in compression of concrete (crushing failure), and the shear failure with the propagation of inclined cracks may interact between each others or a failure may predominate over the others depending on scale, beam span and reinforcement area.

Furthermore, the routine *ReinforcementData.m* may be modified in order to take into account multiple layers reinforcement dispositions with the aim to simulate a more actual steel bars layout.

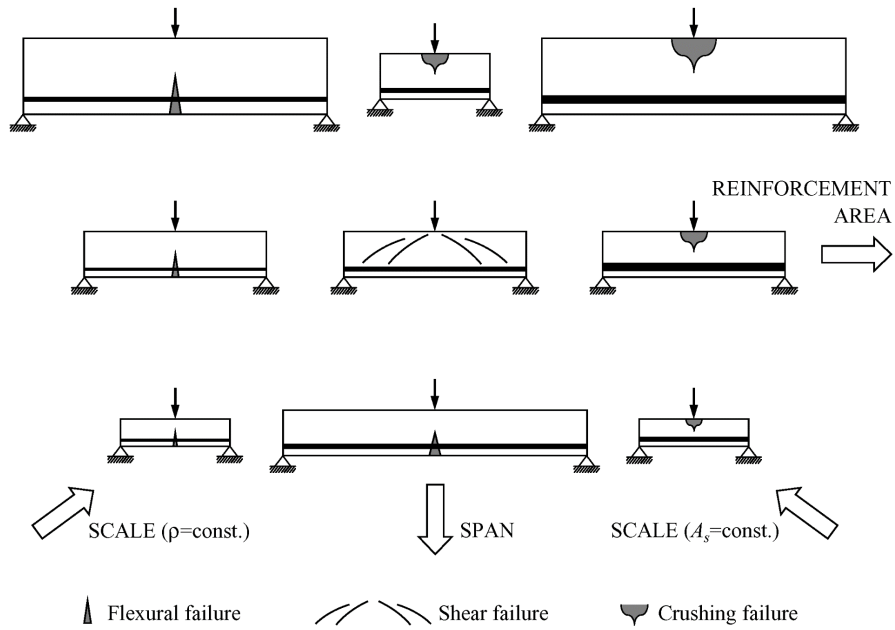


Figure 10.1: Fundamental collapse mechanisms of reinforced concrete beams

As regarding pre-stressed concrete beams, several hypothesis have been introduced, in the present work, since the cohesive crack model and the overlapping crack model have never been used to analyze this type of structures. The results herein presented, however, demonstrate the necessity and the deserving of further detailed studies and a better evaluation of the pre-stressing effect by means of Codes suggestions.

Appendix A

Algorithm Variables

- *fs*: matrix containing, for each step calculation, nodal forces;
- *ws*: matrix containing, for each step calculation, opening/overlapping displacements;
- *thetas*: vector containing, for each step calculation, beam rotations;
- *Ms*: vector containing, for each step calculation, external bending moment;
- *deltas*: vector containing, for each step calculation, beam displacements;
- *fos*: vector containing, for each step calculation, external loads;
- *ntipts*: vector containing, for each step calculation, fictitious cohesive tip positions;
- *ntipats*: vector containing, for each step calculation, real cohesive tip positions;
- *ntipcs*: vector containing, for each step calculation, fictitious overlapping tip positions;
- *ntipacs*: vector containing, for each step calculation, real overlapping tip positions;
- *nstep*: vector containing the number of steps used in the calculation;
- *inoda*: vector containing the nodes positions;

- *Ast*: vector containing the reinforcement/ pre-stressing steel area;
- *ft*: tensile strength of concrete;
- *wct*: threshold fracture opening value;
- *fc*: compressive strength of concrete;
- *wcc*: threshold overlapping value;
- *data*: if the flag *press* = 0, it is a matrix containing in the first column the node list, in the second column the reinforcement diameter and in the third column the number of bars. If the flag *press* = 1, it is a vector containing in the first position the node number where tendon is placed and in the second position the value of the pre-stressing force;
- *span*: beam span value expressed in *mm*;
- *thickness*: beam thickness value expressed in *mm*;
- *heigh*: beam depth value expressed in *mm*;
- *E*: concrete modulus of elasticity expressed in *MPa*;
- *I*: beam inertia expressed in mm^4 ;
- *crushing*: flag that is equal to 1 if the user selects to take into account the concrete crushing otherwise it is equal to 0;
- *rein*: flag that is equal to 1 if a reinforced element is analyzed otherwise its value is equal to 0;
- *Fp*: variable containing the value of the pre-stressing force expressed in *N*;
- *pres*: flag that is equal to 1 if a pre-stressing force is present otherwise its value is fixed to 0;
- *wy*: variable containing the value of the crack opening generating the steel yielding;
- *IndexAs*: variable containing the reinforcement layer nodal position;

- *fut*: ultimate tensile nodal strength;
- *fuc*: ultimate compressive nodal strength;
- *IndexYielded*: flag containing the steel layer status. It is equal to 0 if in the current step calculation, reinforcement does not reach yielding; it is equal to 1 if in the current step calculation, steel reaches yielding; it is equal to 2 if the steel is yielded;
- *Es*: steel modulus of elasticity;
- *tau*: stresses that exchange concrete and steel;
- *diameter*: vector containing the diameter of bars located in each layer;
- *numbar*: vector containing the number of bars located in each layer;
- *n*: homogenization coefficient;
- *A*: cross sectional area of the beam;
- *S*: first moment of the section;
- *y_g*: centroid position of the cross section;
- *coer*: variable that contains the reinforcement effect. In the case of a prestressing force, it is a vector containing the nodal forces generated by F_p ;
- *coe*: matrix containing the elastic coefficients for nodal displacement due a unit force;
- *c*: vector containing the elastic coefficients for nodal displacement due a unit external bending moment;
- *dcoe*: vector containing the rotation generated by a unit nodal force;
- *dc*: variable containing the rotation generated by a unit bending moment;
- *ncort*: variable containing the length of the cohesive process zone;
- *ncorc*: variable containing the length of the overlapping process zone;

- *fold*: variable containing the nodal forces value calculated in the actual crack/overlapping configuration with the load of the previous step calculation;
- *flag*: flag that if equal to 0 does not allow the calculation of the crack opening/ overlapping by the routine *soluz.m*. This flag is used by the function *LoadComputation.m* to save time machine. Consequently, the flag is set equal to 1;
- *cru*: flag that is equal to 0 if, in the actual step calculation, the ultimate tensile strength is reached and equal to 1 if the ultimate compressive strength is reached;
- *M*: variable containing the external bending moment of the actual step calculation;
- *theta*: variable containing the rotation for the actual step calculation;
- *f*: vector containing nodal forces values for the actual step calculation;
- *w*: vector containing the opening/ overlapping displacements for the actual step calculation;
- *del*: vector containing the step calculations for which the convergence of the solution has been lost.

Bibliography

- [1] C. Inglis. “Stress in a plate due to the presence of sharp corners and cracks”. In: *Trans. Roy. Inst. Naval Architects* 60 (1913), pp. 219–241.
- [2] Griffith A. A. “VI. The phenomena of rupture and flow in solids”. In: *Philosophical transactions of the royal society of london. Series A, containing papers of a mathematical or physical character* 221.582-593 (1921), pp. 163–198.
- [3] H. M. Westergaard. “Bearing pressures and cracks”. In: *Trans AIME, J. Appl. Mech.* 6 (1939), pp. 49–53.
- [4] M. L. Williams. “Stress singularities resulting from various boundary conditions in angular corners of plates in extension”. In: *Journal of applied mechanics* 19.4 (1952), pp. 526–528.
- [5] T. L. Anderson. *Fracture mechanics: fundamentals and applications*. CRC press, 2017.
- [6] A. Carpinteri. “Size effects on strength, toughness, and ductility”. In: *Journal of Engineering Mechanics* 115.7 (1989), pp. 1375–1392.
- [7] A. Carpinteri. “Interpretation of the Griffith Instability as a Bifurcation of the Global Equilibrium”. In: *Application of Fracture Mechanics to Cementitious Composites* (1985), pp. 287–316.
- [8] R. L’Hermite. *What do we know about plastic deformation and creep of concrete?* Waterways Experiment Station, 1960.
- [9] H Rusch and H Hilsdorf. “Deformation characteristics of concrete under axial tension”. In: *Voruntersuchungen, Bericht* 44 (1963).
- [10] B. P. Hughes and G. P. Chapman. “The complete stress-strain curve for concrete in direct tension”. In: *Matls & Structures, Res & Testing/Fr/* (1966).

- [11] R.H. Evans and M.S. Marathe. “Microcracking and stress-strain curves for concrete in tension”. In: *Materials and Structures* 1.1 (1968), pp. 61–64.
- [12] A. Carpinteri et al. “Cohesive crack model description of ductile to brittle size-scale transition: dimensional analysis vs. renormalization group theory”. In: *Engineering fracture mechanics* 70.14 (2003), pp. 1809–1839.
- [13] D. C. Drucker. “Some implications of work hardening and ideal plasticity”. In: *Quarterly of Applied Mathematics* 7.4 (1950), pp. 411–418.
- [14] G. Maier. “Incremental plastic analysis in the presence of large displacements and physical instabilizing effects”. In: *International Journal of Solids and Structures* 7.4 (1971), pp. 345–372.
- [15] G. Maier. “Behavior of elastic-plastic trusses with unstable bars”. In: *Journal of the Engineering Mechanics Division* 92.3 (1966), pp. 67–94.
- [16] G. Maier, A. Zavelani, and J.-C. Dotreppe. “Equilibrium branching due to flexural softening”. In: *Journal of the Engineering Mechanics Division* 99.4 (1973), pp. 897–901.
- [17] Y.R. Rashid. “Ultimate strength analysis of prestressed concrete pressure vessels”. In: *Nuclear engineering and design* 7.4 (1968), pp. 334–344.
- [18] G. I. Barenblatt. “The formation of equilibrium cracks during brittle fracture. General ideas and hypotheses. Axially-symmetric cracks”. In: *Journal of Applied Mathematics and Mechanics* 23.3 (1959), pp. 622–636.
- [19] G. I. Barenblatt. “The mathematical theory of equilibrium cracks in brittle fracture”. In: *Advances in applied mechanics*. Vol. 7. Elsevier, 1962, pp. 55–129.
- [20] D. S. Dugdale. “Yielding of steel sheets containing slits”. In: *Journal of the Mechanics and Physics of Solids* 8.2 (1960), pp. 100–104.
- [21] A. Hillerborg, M. Modéer, and P.E. Petersson. “Analysis of crack formation and crack growth in concrete by means of fracture mechanics and finite elements”. In: *Cement and concrete research* 6.6 (1976), pp. 773–781.
- [22] A. Carpinteri et al. “The overlapping crack model for uniaxial and eccentric concrete compression tests”. In: *Magazine of Concrete Research* 61.9 (Nov. 2009), pp. 745–757. ISSN: 1751-763X.

- [23] A. Carpinteri et al. “New Model for the Analysis of Size-Scale Effects on the Ductility of Reinforced Concrete Elements in Bending”. In: *Journal of Engineering Mechanics* 135.3 (Mar. 2009), pp. 221–229. ISSN: 1943-7889.
- [24] A. Carpinteri et al. “Il modello della fessura coesiva in trazione e compressione per la valutazione della duttilità degli elementi strutturali in calcestruzzo armato”. In: *Frattura ed Integrità Strutturale* 3.7 (Jan. 2009), pp. 17–28.
- [25] A. Carpinteri and M. Corrado. “Dimensional analysis approach to the plastic rotation capacity of over-reinforced concrete beams”. In: *Engineering Fracture Mechanics* 77.7 (May 2010), pp. 1091–1100. ISSN: 0013-7944.
- [26] A. Carpinteri and M. Corrado. “Nonlinear fracture mechanics investigation on the ductility of reinforced concrete beams”. In: *Revista IBRACON de Estruturas e Materiais* 3.2 (June 2010), pp. 137–148. ISSN: 1983-4195.
- [27] A. Carpinteri, M. Corrado, and M. Paggi. “An integrated cohesive/overlapping crack model for the analysis of flexural cracking and crushing in RC beams”. In: *International Journal of Fracture* 161.2 (Feb. 2010), pp. 161–173. ISSN: 1573-2673.
- [28] A. Carpinteri, M. El-Khatieb, and E. Cadamuro. “Failure mode transitions in RC beams: A cohesive/overlapping crack model application”. In: *Meccanica* 48.10 (May 2013), pp. 2349–2366. ISSN: 1572-9648.
- [29] M. Corrado. “Effetti di scala sulla capacità di rotazione plastica di travi in calcestruzzo armato”. PhD thesis. PhD thesis, Politecnico di Torino, 2007, 164 pp.(in Italian), 2007.
- [30] A. Carpinteri. “Cusp catastrophe interpretation of fracture instability”. In: *Journal of the Mechanics and Physics of Solids* 37.5 (1989), pp. 567–582.
- [31] P.-E. Petersson. “Crack growth and development of fracture zones in plain concrete and similar materials”. English. Defence details Date: 1981-12-04 Time: 13:15 Place: sektionen för Väg och Vatten, John Ericssons väg 1, sal V. PhD thesis. Division of Building Materials, 1981.
- [32] CEB-FIP Model Code. “Model code for concrete structures”. In: *Comité Euro-International du Béton, Secretariat Permanent, Case Postale 88* (1990).

- [33] A. Carpinteri et al. “Numerical simulation of concrete fracture through a bilinear softening stress-crack opening displacement law”. In: *Fracture of Concrete and Rock*. Springer, 1989, pp. 131–141.
- [34] A. Carpinteri. “Post-peak and post-bifurcation analysis of cohesive crack propagation”. In: *Engineering Fracture Mechanics* 32.2 (1989), pp. 265–278.
- [35] J. Planas and M. Elices. “Un nuevo metodo de analisis del comportamiento de una fisura cohesiva en Modo I”. In: *Anales de Mecanica de la Fractura* 3 (), pp. 219–227.
- [36] J. Planas and M. Elices. “Asymptotic analysis of a cohesive crack: 1. Theoretical background”. In: *International Journal of Fracture* 55.2 (May 1992), pp. 153–177. ISSN: 1573-2673.
- [37] Z. P. Bažant. “Smearred-tip superposition method for nonlinear and time-dependent fracture”. In: *Mechanics Research Communications* 17.5 (Sept. 1990), pp. 343–351. ISSN: 0093-6413.
- [38] Z. P. Bažant. *Fracture and size effect in concrete and other quasibrittle materials*. Routledge, 2019.
- [39] Z. P. Bažant and S. Beissel. “Smearred-tip superposition method for cohesive fracture with rate effect and creep”. In: *International Journal of Fracture* 65.3 (1994), pp. 277–290.
- [40] Z. P. Bažant and Y. Xiang. “Size effect in compression fracture: splitting crack band propagation”. In: *Journal of engineering mechanics* 123.2 (1997), pp. 162–172.
- [41] A. Carpinteri, G. Ferro, and I. Monetto. “Scale effects in uniaxially compressed concrete”. In: *Mag. Concr. Res* 51.3 (1999), pp. 217–225.
- [42] J. G. M. Van Mier. *Strain-softening of concrete under multiaxial loading conditions*. Citeseer, 1984.
- [43] M. R. A. van Vliet and J. G. M van Mier. “Experimental investigation of concrete fracture under uniaxial compression”. In: *Mechanics of Cohesive-frictional Materials: An International Journal on Experiments, Modelling and Computation of Materials and Structures* 1.1 (1996), pp. 115–127.
- [44] D. C. Jansen and S. P. Shah. “Effect of length on compressive strain softening of concrete”. In: *Journal of Engineering Mechanics* 123.1 (1997), pp. 25–35.

- [45] G. Ferrara and M. E. Gobbi. “Strain softening of concrete under compression”. In: *Report to RILEM Committee* 148 (1995).
- [46] A. Carpinteri et al. “The overlapping crack model for uniaxial and eccentric concrete compression tests”. In: *Magazine of Concrete Research* 61.9 (2009), pp. 745–757.
- [47] A. Carpinteri et al. “Cohesive versus overlapping crack model for a size effect analysis of RC elements in bending”. In: *Proceedings of FraMCoS-6, Catania, Italy* (2007), pp. 655–663.
- [48] A. Carpinteri et al. “A numerical approach to modelling size effects on the flexural ductility of RC beams”. In: *Materials and Structures* 42.10 (Dec. 2009), pp. 1353–1367. ISSN: 1871-6873.
- [49] A. Hillerborg. “Fracture mechanics concepts applied to moment capacity and rotational capacity of reinforced concrete beams”. In: *Engineering Fracture Mechanics* 35.1-3 (1990), pp. 233–240.
- [50] H. Dahl and R. Brincker. “Fracture energy of high-strength concrete in compression”. In: *Fracture of concrete and rock—recent developments. Proceedings of the international conference on recent developments in the fracture of concrete and rock, Cardiff, Wales*. 1989, pp. 523–536.
- [51] G. Ferro and A. Carpinteri. “Effect of Specimen Size on the Dissipated Energy Density in Compression”. In: *Journal of Applied Mechanics* 75.4 (2008), p. 041003. ISSN: 0021-8936.
- [52] M. Suzuki et al. “Concentric loading test of RC columns with normal-and high-strength materials and averaged stress-strain model for confined concrete considering compressive fracture energy”. In: *Proceedings of the 2nd fib Congress, Naples, Italy*. 2006, pp. 5–8.
- [53] R.L. Taylor. *FEAP-A finite element analysis program*. 2014.
- [54] G. Ruiz and J. Planas. “Propagación de una fisura cohesiva en vigas de hormigón débilmente armadas: modelo de la longitud efectiva de anclaje”. In: *Anales de Mecánica de la Fractura*. Vol. 11. 1994, pp. 506–513.
- [55] G. Ruiz, J. Planas, and M. Elices. “Propagación de una fisura cohesiva en vigas de hormigón débilmente armadas”. In: *Anales de Mecánica de la Fractura*. Vol. 10. 1993, pp. 141–146.

- [56] G. Ruiz. “Propagation of a cohesive crack crossing a reinforcement layer Propagation of a cohesive crack crossing a reinforcement layer”. In: *International Journal of Fracture* 111.3 (2001), pp. 265–282. ISSN: 0376-9429.
- [57] G. Ruiz, M. Elices, and J. Planas. “Size Effect and Bond-Slip Dependence of Lightly Reinforced Concrete Beams”. In: *European Structural Integrity Society* (1999), pp. 67–97. ISSN: 1566-1369.
- [58] Model Code. “Fib model code for concrete structures 2010”. In: *Document Competence Center Siegmund Kästl eK, Germany* (2010).
- [59] A. Carpinteri. *Development of realistic concrete models including scaling effects*. Tech. rep. Commission of the European Communities, 1989.
- [60] A. Carpinteri et al. “Scale Effects and Transitional Failure Phenomena of Reinforced Concrete Beams in Flexure”. In: *European Structural Integrity Society* (1999), pp. 1–30. ISSN: 1566-1369.
- [61] TC RILEM. “FMC 1 Determination of the fracture energy of mortar and concrete by means of three-point bend tests on notched beams, 1985”. In: *RILEM Recommendations for the Testing and Use of Construction Materials* (1994), pp. 99–101.
- [62] A. Carpinteri, E. Cadamuro, and M. Corrado. “Minimum flexural reinforcement in rectangular and T-section concrete beams”. In: *Structural Concrete* 15.3 (2014), pp. 361–372.
- [63] A. Carpinteri. “Snap-back and hyperstrength in lightly reinforced concrete beams”. In: *Magazine of Concrete Research* 40.145 (1988).
- [64] S. J. Seguirant, R. Brice, and B. Khaleghi. “Making sense of minimum flexural reinforcement requirements for reinforced concrete members.” In: *PCI journal* 55.3 (2010).
- [65] *Eurocode 2. Design of concrete structures*.
- [66] British Standard Committee et al. “British Standard Code: Design of Concrete Structures (BS 8110-1: 1997)”. In: *British Standards* (1997).
- [67] ACI Committee and International Organization for Standardization. “Building code requirements for structural concrete (ACI 318-08) and commentary”. In: American Concrete Institute. 2008.

- [68] Standard Australia. “Australian Standard for Concrete Structures AS 3600-2001”. In: (2001).
- [69] IS Indian Standard. “IS 456 2000: Plain and Reinforced Concrete. Code of Practice (4th revision)”. In: *New Delhi* (2000).
- [70] Norwegian Code. *NS 3473 E. Concrete structures design rules*. 1992.
- [71] A. Carpinteri. *Minimum reinforcement in concrete members*. Vol. 24. Elsevier, 1999.
- [72] C. Bosco and A. Carpinteri. “Fracture mechanics evaluation of minimum reinforcement in concrete structures”. In: *Applications of fracture mechanics to reinforced concrete* (1992), pp. 347–377.
- [73] N.M. Hawkins and K. Hjortset. “Minimum Reinforcement Requirements for Concrete Flexural Members”. In: *Applications of fracture mechanics to reinforced concrete* (1992), p. 379.
- [74] W. H. Gerstle et al. “Crack Growth in Flexural Members—A Fracture Mechanics Approach”. In: *Structural Journal* 89.6 (1992), pp. 617–625.
- [75] M.H. Baluch and K. Azad. *Fracture Mechanics Application to Reinforced Concrete Flexural Member*. CRC Press, 1992, p. 413.
- [76] G. A. Rao, J. Aravind, and R. Eligehausen. “Evaluation of minimum flexural reinforcement in RC beams”. In: *Journal of Structural Engineering* 34.4 (2007), pp. 277–283.
- [77] I.A.E.M. Shehata, L.C.D. Shehata, and S.L.G. Garcia. “Minimum steel ratios in reinforced concrete beams made of concrete with different strengths—Theoretical approach”. In: *Materials and Structures* 36.1 (Jan. 2002), pp. 3–11. ISSN: 1871-6873.
- [78] E. Buckingham. *Model experiments and the forms of empirical equations*. Verlag nicht ermittelbar, 1915.
- [79] C. Bosco, A. Carpinteri, and P.G. Debernardi. “Minimum reinforcement in high-strength concrete”. In: *Journal of Structural Engineering* 116.2 (1990), pp. 427–437.
- [80] E. Siviero. “Rotation capacity of monodimensional members in structural concrete”. In: *CEB Bulletin d’information* 105 (1974), pp. 206–222.

- [81] R. Eligehausen and P. Langer. “Rotation capacity of plastic hinges and allowable degree of moment redistribution”. In: (1987).
- [82] M. Corrado, M. Paggi, and A. Carpinteri. “Cohesive-overlapping crack model describing the size-scale effects on the rotational capacity of RC beams in bending”. In: *Fracture Mechanics of Concrete Structures* (2010), pp. 183–190.
- [83] A. Carpinteri and M. Corrado. “Upper and lower bounds for structural design of RC members with ductile response”. In: *Engineering Structures* 33.12 (2011), pp. 3432–3441.

